UNIVERSITY OF CALIFORNIA SAN DIEGO

Charge transfer study in nanostructure and biological redox pathway

A dissertation submitted in partial satisfaction of the
requirements for the degree
Doctor of Philosophy

in

Materials Science and Engineering

by

Peng Chen

Committee in charge:

Prabhakar R. Bandaru, Chair
Matthew Baldwin
Shadi A. Dayeh
Dimitri D. Deheyn
David Fenning
Javier Garay
Yu-hwa Lo

2020

The dissertation of Peng Chen is approved, and it is acceptable in quality and form for publication on microfilm and electronically:

_____

_____

_____

_____

Chair

University of California San Diego

2020

DEDICATION

To my hunsbad, my best friend **Hongyi Yao** who gives me supports to all my challenging choices and deals with all kinds of difficulties together with me;

To my parents who encouraged me to pursue my dreams;

To my academic adviser who guided me and the committee who kept me on track.

EPIGRAPH

A careful quotation

conveys brilliance.

—Smarty Pants

TABLE OF CONTENTS

LIST OF FIGURES

ACKNOWLEDGEMENTS

First and foremost, I would like to thank my advisor, Prof. Prabhakar R. Bandaru. I appreciate all his contributions of time, ideas, and funding to make my Ph.D. experience productive. Prof. Bandaru has given me the freedom to pursue various projects and connected me with various researchers. I've learnt a lot from him not only for research aspects but also the way to analyze and solve problems. I especially appreciate his guidance on the physics modeling and the way to evaluate problems. I also want to thank him for the training on my presentation skills. I made breakthrough in the path of meeting his high standard. He is not only a good researcher but also really a wonderful educator with patient and enthusiasm.

Next, I would like to thank my dissertation committee members, Dr. Matthew Baldwin, Dr. Shadi A. Dayeh, Dr. Dimitri D. Deheyn, Dr. David Fenning, Dr. Javier Garay and Dr. Yu-hwa Lo for their time, interest, and valuable comments about my research. It is a pleasure to work with Dr. Matthew Baldwin to prepare tungsten sample with He plamsa. And I'm so glad to have this opportunity to explore this new material. I would like to thank the great patience and enthusiasm of Dr. Dimitri D. Deheyn. For the innovative ferritin project, the encouragement and valuable solutions from Dr. Deheyn helps me during the tough time.

I would like to thank Dr. E. D. Meulenaere. Evelien is a biochemist and ocean scientist, and we work on the ferritin project together. I treasure the time we discussed over hours or through hundreds of emails, and also the inspiring ideas during that time. Beyond research, Evelien also guides me to the beautiful ocean world, and shows me magic creatures.

I want to thank my group members. I'm very appreciate the valuable discussion with Dr. H. Yamada, Dr. R. Narayanan. They are so helpful for me to develop my own theory. Also thanks E. Martinez for always willing to help and discuss. Thanks to Dr. Bei Fan, Nirjhar Sarkar and Dr. A. Alexander,for their help and support for all the projects.

I would like to thank my friends at UCSD, they are excellent at work and have adorable personalities, Yun Zhou, Yangting Sun, Zichen Zhang, Dr. Shuang Cui, Qingqing Yang, Yang Shi,

Jian Zeng, Yanjie Jiang, Yanzeng Zhang, Rui Kou, Qingyang Wang, Xuan Feng, Yangyuchen Yang et al. They made me feel like home for the lonely and hard time.

I would like to specially thank my husband, Hongyi Yao, for his support, understanding, long time patience and accompanying. We met each other 2009. For 10 years, we share all the happy, exciting, challenging, sad even desperate moments. I'm so glad we went through the over six years long distance relationship.

The material in this dissertation is based on the following papers which are published.

Portion of chapter 2 has been published on Journal of Materials Chemistry A in 2017, "Hierarchically structured, oxygen deficient, tungsten oxide morphologies for enhanced photo-electrochemical charge transfer and stability.", by Chen, P., M. Baldwin, and P. R. Bandaru. The authors are grateful for support from the Defense Advanced Research Projects Agency (DARPA: W911NF-15-2-0122) and the National Science Foundation (NSF: CBET 1606192 and CMMI 1246800). The discussions with H. Yamada, R. Narayanan, and E. Martinez are appreciated.

Portion of charpter 3 "Static and dynamic charging characteristics of nanoscale fuzzy tungsten surfaces." by Chen, P., J. Sigurdson, M. Baldwin, and P. R. Bandaru is under revision. This work was supported by a grant (CBET 1606192) from the National Science Foundation (NSF). P.C. and P.R.B. contributed to the conceptualization, experimental design, and the development of the project. P.C. carried out the electrochemical measurements, while P.C. and M.B. synthesized the fuzzy tungsten samples. P.C. and P.R.B. wrote the paper.

Portion of charpter 4 has been accepted by Scitific Report 2020 "Iron redox pathway revealed in ferritin via electron transfer analysis" by Chen, P., E. D. Meulenaere, D. D. Deheyn, P. R. Bandaru The authors are grateful for support from the National Science Foundation (NSF: CBET 1606192, to P.R.B.) and from the Air Force Office of Scientific Research (AFOSR FA9550-17-0189, to D.D.D.). We acknowledge Prof. J. Day at the Scripps Isotope Geochemistry Laboratory for performing the ICP-MS measurements. D.D.D. came up with the original research question. All authors formulated together the research design and contributed to data interpretation.

E.D.M. performed all cloning, expression and purification work in D.D.D. lab. P.C. performed all voltammetry-related work in P.R.B. lab.

VITA

2009-2013	B. S. in Materials Science University of Science and Technology of China, China
2014-2015	M. S. in Materials Science and Engineering University of Augsburg, Germany
2014-2015	M. S. in Materials Science and Engineering University of Bordeaux, France
2015-2020	Ph. D in Materials Science and Engineering University of California, San Diego

PUBLICATIONS

Chen, P., M. Baldwin, and P. R. Bandaru. Hierarchically structured, oxygen deficient, tungsten oxide morphologies for enhanced photoelectrochemical charge transfer and stability.**Journal of Materials Chemistry A** 5.28 (2017): 14898-14905.

Chen, P., E. D. Meulenaere, D. D. Deheyn, P. R. Bandaru.Iron redox pathway revealed in ferritin via electron transfer analysis. **Sci Rep** 10, 4033 (2020).

Chen, P., J. Sigurdson, M. Baldwin, and P. R. Bandaru. Static and dynamic charging characteristics of nanoscale fuzzy tungsten surfaces. (under revision)

ABSTRACT OF THE DISSERTATION

Charge transfer study in nanostructure and biological redox pathway

by

Peng Chen

Doctor of Philosophy in Materials Science and Engineering

University of California San Diego, 2020

Prabhakar R. Bandaru, Chair

The probe of charging transfer (CT) process can be of vita importance in various fields, including energy generation, energy storage and investigating biological processes.This dissertation focuses on the development of methodology to study complex CT proceses via electrochemical characterization. The static and dynamic charging characterization, oxygen deficiency impact on the CT process as well as performance of non-stoichiometric nanostructured tungsten oxide will be discussed. Additionally, in the aspect of biological process, the iron redox pathway in ferritin is revealed via electrochemical analysis.

Chapter 1

Introduction

For the past decades, researchers in different areas, ranging from biology to electronics, have made efforts to understand and utilize charge transfer processes to energy conversion. Electrical engineering and materials scientists utilize semiconductor to convert solar energy directly to generate electricity or store chemical energy in the form of hydrogen. When light shines on the semiconductor, electron-hole pairs (e-h) are generated on semiconductor surface and once e-h can be guided to separate and utilized to split water into hydrogen and oxygen. Since the most electrical/photoelectrical chemical processes take place at the interface of semiconductor/liquid, this highly interdisciplinary field needs thorough understanding in electrochemistry, interfacial charge transfer in physical chemistry and electronic band structure, optoelectronic effects in semiconductor physics[1].

Interestingly, light-electricity conversion stories also take place in biology kingdom. Instead of generating electricity from light, it also works reversely – light emission triggered by utilizing electricity. A recent study[2] reported that a long term glow in a marine worm named Chaetopterus[3]. The biochemical reaction behind this light emission can be associated with the Fe^{3+}/Fe^{2+} electron transition inside ferritin. Unlike electron exchange for inorganic redox, the process in enzyme becomes challenging due to the fact that the active site of proteins is deeply

buried in the protective protein matrix.[4, 5]

The purpose of this thesis is to reveal the complex charge transfer processes in energy conversion by utilizing electrochemical tools. The theoretical context is well explained in Chapter 2. Chapter 3 is focused on our research about improving energy conversion efficiency and stability via introducing oxygen deficiency. We also developed methodology to understand and evaluate PEC performance with bandstructure considerations. In Chapter 4 we go further to understand the charge transfer and storage in nanostructures. Our analyses on surface charge density combine electrochemical techniques and surface wetting properties, and both static and dynamic charging are taken into consideration. At last, the exploration of biological charge transfer study inside ferritin are demenstrated in Chapter 5. For this complex situation, we deployed differential pulse voltammetry (DPV) to probe the transient current change at the interface of electrode and pretein shell. It's the first time to tailor biochemical charge transfer mechanism via integrating DPV analyses. Our results open the door to more applied research where directed changes of specific residues could be used to increase performance of human ferritin

Chapter 2

Theory

2.1 Electrical and photoelectrical properties of semiconducting metal oxides

If a more negative voltage is applied, the inversion voltage V_{INV} is reached when the concentration of holes and electrons at the semiconductor surface is equal. The inversion layer is formed in figure 2.1C as soon as the Fermi level at the electrode surface, E_F, crosses the intrinsic Fermi level E_i. If the applied potential of the p-type semiconductor continues to decrease the surface reaches a situation where there are more minority carrier electrons than majority carrier holes; this is weak inversion. If the band bending keeps pushing up, a strong conversion will reach at $\Phi_s > 2\Phi_F$(Φ_F is flat band potential).

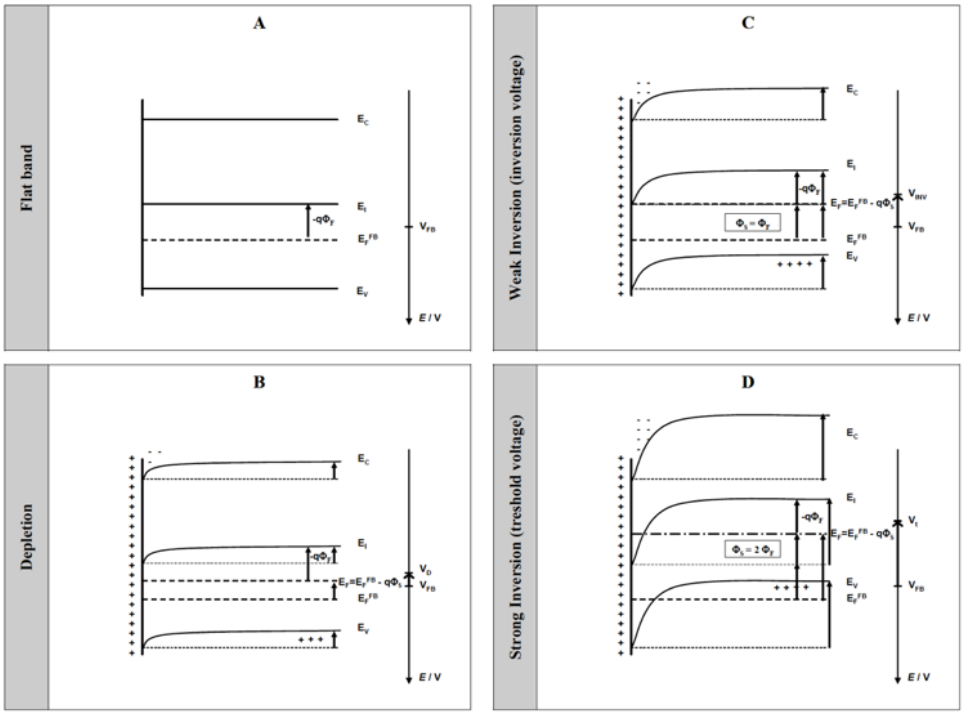

Figure 2.1: Band bending for different polarizations of a p-type semiconductor electrode. E (in italics) is the electrochemical potential in volts and E is the energy in electron-volts. A, B, C and D correspond to four regimes, flat band, depletion, weak inversion and strong inversion, respectively.

2.2 Thermodynamic potentials of semiconductors in aqueous solution

A challenging issue for water splitting not for the photovoltaic cells is the photo-induced corrosion. For example, for a n-type semiconductor with VB lower than $\Phi(O_2/H_2O)$, the photo-generated holes (h^+) may oxidize the semiconductor first, rather than the water. S. Chen and L. Wang[6] predicted the stability of most compound semiconductor in aqueous solution by calculating the compound formation energy since experimental Gibbs free energy is not reported for specific compound and band alignment with electrochemistry experimental data.

Whether the semiconductor is resistant to the photocorrosion depends on the alignment of oxidation potential related to $\Phi(O_2/H_2O)$, and reduction potential relative to $\Phi(H^+/H^2)$. If the

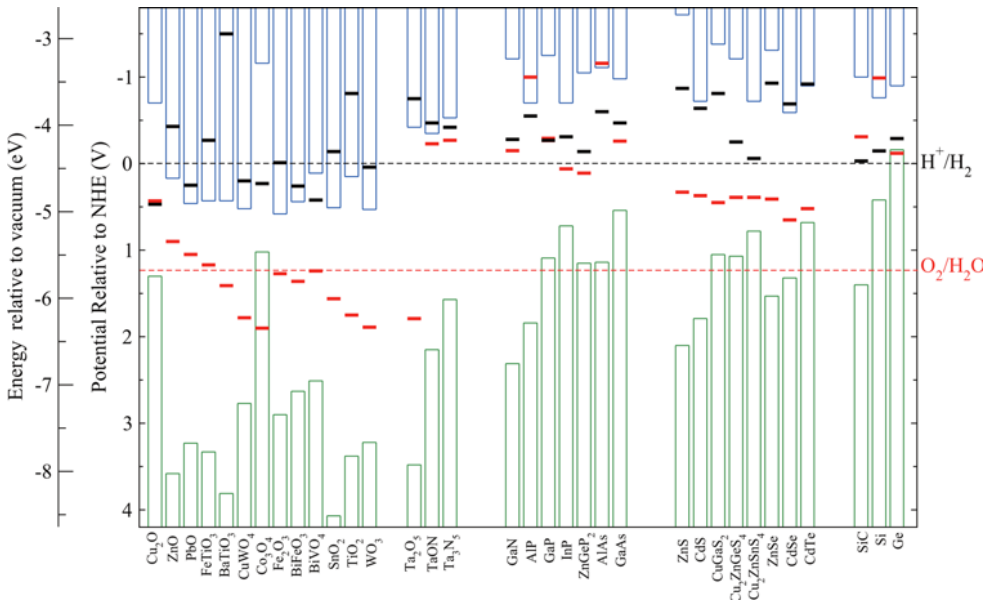

Figure 2.2: Calculated oxidation potential (red bars) and reduction potential (black bars) relative to the NHE and vacuum level for a series of semiconductors in solution at pH = 0[6]

conduction band minimum (blue column) and reduction potential (black bar) of a semiconductor are both higher than $\Phi(H^+/H^2)$ (black dashed line), it can be a stable photocathode against reduction, and if the valence band maximum (green column) and oxidation potential (red bar) are both lower than $\Phi(O_2/H_2O)$ (red dashed line), the semiconductor can be a stable photoanode against oxidation. According to their calculation results, the reported non-oxide semiconductor photoanodes they calculated are unstable due to easy oxidation by photo-generated holes.

2.3 Characterization methods in the study of oxygen vacancies

Electrochemical impedance spectroscopy (EIS) is a powerful tool to study the interface between the semiconductor and electrolyte. Related resistance and capacitance information can be derived from EIS results. The impedances Z are measured at different angular frequencies. The window of frequencies provides the relevant information about resistances and capacitances for a

given process. These values can be further interpreted with the equivalent circuit (EC). However, since many types of ECs can be applied to one data set, it sometimes becomes ambiguous for interpreting the results. Thus, a plausible model needs to be established before applying EC.

However, except for the impedance formed by charge transfer resistance and double layer capacitance, an additional component – surface states play varied roles and makes it difficult to interpret EIS. As we discussed before, the surface states in PEC systems may have contrasting advantages and disadvantages: These states can facilitate the charge transfer of holes to the donor species in solution; however, without optimized band modulation they also work as recombination centers – trapping electrons from the conduction band and holes from the valence band eventually decreasing the photocurrent.

2.4 Thermodynamic potentials of semiconductors in aqueous solution

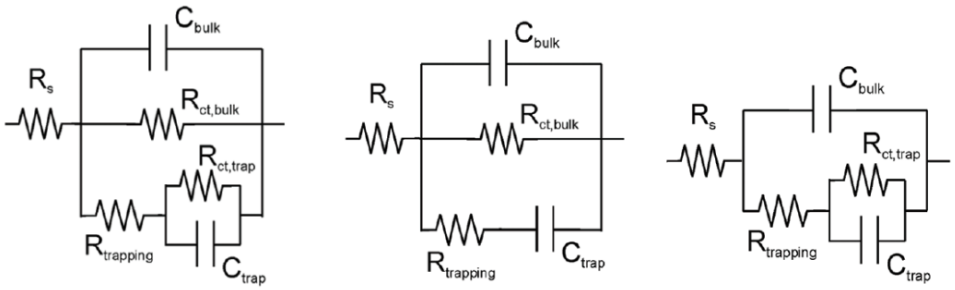

Figure 2.3: Physical models for the dynamics: left figure Equivalent circuit considering all the components, while in the middle is the equivalent circuit for the charge transfer from the valence band – removing $R_{ct,trap}$; and on the right is the charge transfer from the surface states – removing $R_{ct,bulk}$.

Through providing impedance information on semiconductor/liquid interface, EIS is a powerful tool for investigating the charge transfer processes at these surface states. Employing impedance spectroscopy, B. Klahr et al.[7] proposed a general model on hematite to discuss

the surface states at the semiconductor/ liquid interface. Based on the Randles circuit, they established a model considering all possible pathways for charge transfer. First, they assumed the major pathway for charge transfer inside the bulk semiconductor, which in E_C model can be represented by bulk charge transfer resistance $R_{ct,bulk}$ and bulk capacitance C_{bulk} connected in parallel. The surface states, as the recombination center, provide another pathway for charge transfer, thus the trapping resistance $R_{trapping}$ is added in parallel. The other possibility is charge transfer taking place at the surface states. In this case, two elements – $R_{ct,trap}$ and C_{trap} are added (Figure 2.3(a)). Then to simplify the model, they either removed $R_{ct,trap}$ for valence band charge transfer (figure 2.3(b)) or R_{ct}, bulk for the surface states charge transfer (figure 2.3(c)).

2.5 Electrical and Photoelectrical applications of oxygen deficient tungsten oxides

Tungsten oxide (WO_{3-x}), with the advantage of earth-abundance, high chemical stability and tunable electrical properties, has received great attention. Various applications, such as supercapacitors, Lithium-ion battery, gas sensor and non-volatile memory devices have been investigated.[8, 9] When we come to the fundamental properties, WO_3 crystals are made of perovskite units with a considerable amount of oxygen deficiency. Its electronic band structure and conductivity can be affected by a partial loss of the lattice oxygen[9]. To improve the dynamics of oxygen evolution, hydrogen treatments[10, 11] were introduced to form oxygen vacancies at the surface of WO_3. They found the photocurrent and photostability are much enhanced when oxygen vacancies added. Conventionally, the photocatalysts for hydrogen evolution reaction (HER) are metals or alloys[12]. Platinum is an efficient catalyst, but its high cost and low abundance limit commercial applications. Transition metal oxides become good alternatives, but most of them are unstable in water. Y. Li et al.[13] experimentally observed that the $WO_{2.9}$ with tailored structure exhibits excellent HER activity with a small overpotential.

2.6 Promising applications of non-stoichiometric transition metal oxides

Water splitting Photochemical water splitting is initiated when a semiconductor absorbs light photons with energies greater than its band-gap energy (Eg). This absorption creates excited photoelectrons in the conduction band (CB) and holes in the valence band (VB). Once the photogenerated electron-hole pairs have been created, they separate and migrate to the surface. At the surface of the semiconductor, the photoinduced electrons and holes reduce and oxidize adsorbed water to produce gaseous oxygen and hydrogen.[6, 14] Efforts have been made in two directions: 1. Optimizing the electrode morphology to increase photocurrent density; 2. Employing various surface treatments to reduce the overpotential. The material composition and morphology influence not only the catalyst activity toward the OER, but also its corrosion stability. It happens sometimes that the higher the activity, the lower the stability under typical oxygen evolution conditions. The surface charge recombination can be largely suppressed by electrocatalysts, but the what happens on the electrolyte/semiconductor interface is still a key issue before we fully understand this process.[15]

Resistive Random Access Memory (RRAM) The operation of RRAM, through applying voltage/current pulses, induces a resistance change in the device system. The information can be stored by this resistance change. RRAMs can be classified into two types: 1. Metal cation based electrochemical metallization (ECM) RRAM; 2. Oxygen vacancies based (V_o) RRAM. For ECM, metal cations are much more diffusive than oxygen anions, a conductive metallic bridge is formed in the ON state, which leads to the device from a high resistance state (HRS) to a low resistance state (LRS). On the other hand, V_o based RRAM has a more diffusive oxygen anions, and the nature and of the conductive filament in the ON state is attributed to the traps formed by V_o. In this kind of devices, the SET and RESET operations involve V_o generation and annihilation. When V_o concentration is large, the cell has low resistance; when the V_o

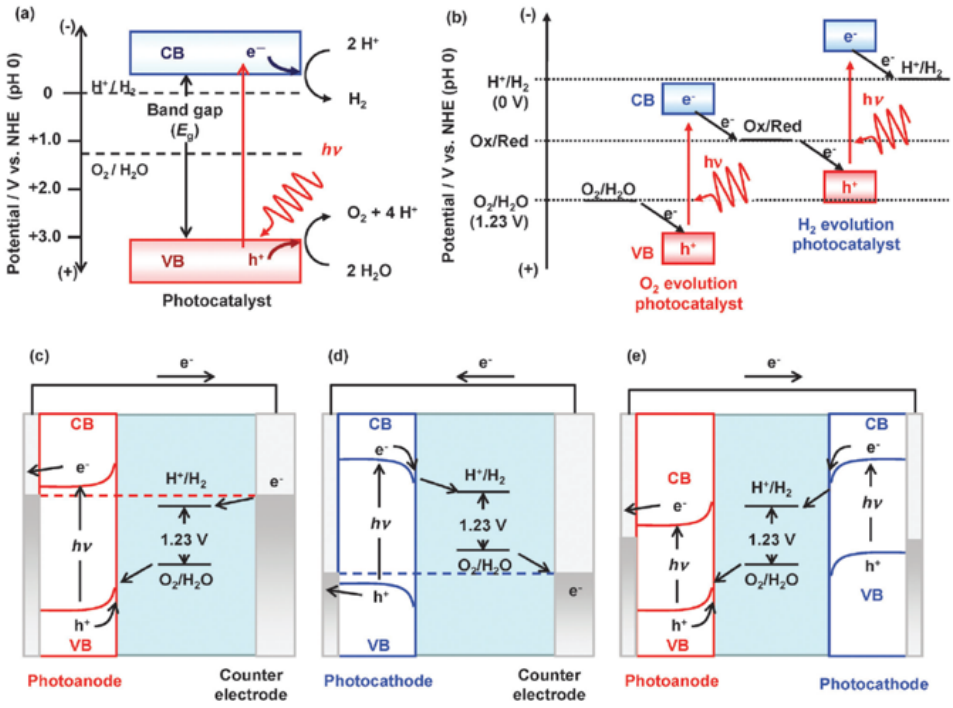

Figure 2.4: Energy diagrams of photocatalytic water splitting based on (a) one-step excitation and (b) two-step excitation; (c) – (e) are photoanode, photocathode and both in tandem configuration.

concentration is low, the cell resistance increases. The main motivation to investigate RRAM is due to its advantages, which almost cover all the merits of an ideal memory such as large endurance, long retention, fast access speed, low power and high density. This operation involves electrochemical processes together with the physical migration of metal cations or oxygen anions.

Persistent photoconductivity The persistent photoconductivity (PPC) is an effect that photoconductivity persists after the illumination, which would hinder the quick recovery of the initial unperturbed state. It implies applications in bistable optical switches and radiation detectors. The PPC phenomenon is related to metastable bulk defects located between shallow and deep energy levels. Some claimed oxygen vacancies can be excited to a metastable charged state after a structural relaxation. And others demonstrate the PPC is directly related to the electron-hole separation near the surface. There is no widely accepted mechanism has been presented. K. Huang et al.[16] reported a WO_3 nanowire device with PPC effect in vacuum and air conditions.

In their results, the photocurrent can hold to 104 seconds in vacuum without decay, while a gradual decreasing current can be found in the air. They concluded the decay in the air of the electronic current can be attributed to the adsorption of oxygen which works as recombination center on the surface.

2.7 Electrochemistry as a tool for the charge transfer studies in biological systems

Electrochemistry is a powerful tool to observe direct charge transfer process.[4] When applying appropriate electrode potential, electrons flow between the active site in protein and the electrode. The consumption of the redox species is detected as a current wave as a result of its electrochemical recycling.[4, 17] Evidences[18] show that redox reactions involving the Fe^{2+}/Fe^{3+} components of the ferritin core can occur without direct interaction of the redox reagent at the mineral core surface. In another word, the long-distance ferritin-redox species electron transfer is possible[18]. Meanwhile, earlier electrochemical experiments performed on heavily iron loaded ferritin[19–22] indicated the possibilities of electrochemical control of iron oxidation states in ferritin. However, due to heavily doping, the iron stored in these ferritin samples are at least 10 times higher than natural case. As ferritin changes its behavior for various iron level[22], results under high iron loading may not be a good representative to the real case.

Extracting detailed information of redox enzymes is never expected to be straightforward. The failure of measurements can be attributed to essential requirements of proteins as well as detection setup[5, 23], such as current is more significant than detection resolution[23], active sites in protein need to be exposed to specific electrode, and signal should not be obscured by non-faradic current. A great advantage of differential voltammetric techniques is enhanced sensitivity, where a relatively small change in the potential may induce a large change in the current, as a result, the detection resolution can be improved to 10^{-7} M[24]. Moreover, taking

the difference of the electrical currents at relatively close values of the voltage in a small time interval, ensures adequate subtraction of the background contributions.

Apart from the difficulties of detection, charge transfer in a redox enzyme, unlike simple reversible redox reaction, can be hard to interpret when coupled with chemical reactions[4, 25]. Aiming at characterizing electrochemical reaction mechanisms, cyclic voltammetry (CV) is the most commonly used method. However, it becomes less applicable for protein study due to low sensitivity and low resolution.[26] Also fast-scan CV has been suggested to capture rapid electron exchange processes.19 Unfortunately, a great aggregation comes about when applying to ferritin.

Specifically, we employ a reductionist approach where the Fe(II)/Fe(III) redox behavior is parameterized in terms of electrons flow between the active site in protein and the electrode[4, 17]. Yet electrons exchange between enzyme and electrode becomes challenging due to the fact that the active site of proteins is deeply buried in the protective protein matrix.[4, 5]. The DPV was employed for obtaining high species-specific sensitivity and incorporates the application of a voltage pulse. Another advantage compared to external redox agents is the potential of the electrode can be continuously swept to provide whichever driving force is required to elicit catalysis that would be a precise control of the redox conditions.[4] Nevertheless, the motivation for such an approach arises from previous studies that (a) direct charge transfer has been applied on various redox enzymes studies, and provided information highly relevant to the mechanism[4, 5, 23], and (b) Long-range electron transfer, mediated through electron tunneling through the ferritin shell has been suggested[27], as evidenced by that large external oxidizing agent, for example, Cytochrome c seems to be as effective as O_2 in the ferritin core.[18]

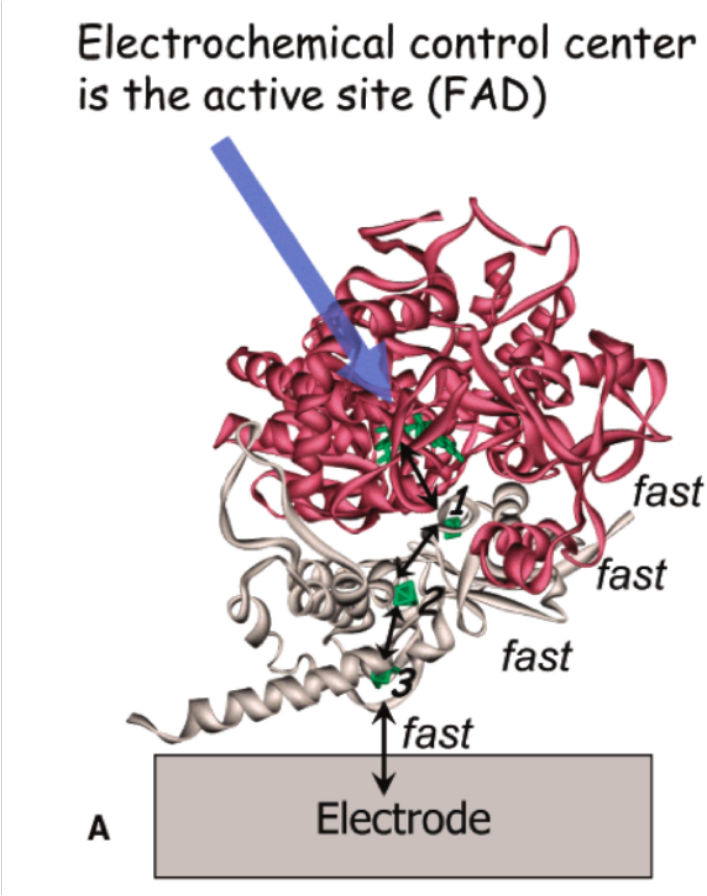

Figure 2.5: Scheme of voltammetry for protein analysis[2]

2.8 The limitation of the ferritin in human and the issues needed to be addressed in iron metabolism or iron related disease

In living system, the vast majority of accurate and high efficient biochemical processes are dependent on the catalytic activities of redox enzymes. Iron is such an essential metal whose role as either a redox center or a Lewis acid in the catalytic sites for enzymes[28]. An understanding of the reduction-oxidation (redox) kinetics of the iron-storage protein – ferritin, is of significant importance for life processes ranging from the uptake of Fe in prokaryotic and eukaryotic organisms[29] as may also be crucial in the interpretation of various metabolic phenomena ranging from oxygen transportation[30–32] to brain function[3, 28]. The essential

role of ferritin is also characterized by both iron deficiency and overload may lead to a distinct disorder even an organ damage. Despite a high stores of body iron, anemia can also be caused by functional iron deficiency due to low circulation iron level. This is in view of the principle, that an efficient Fe transport in and out of ferritin - with a core predominantly constituted from Fe^{3+} incorporated into a compound of the Fe(O)OH type -, has been implicated in the iron release, typically as labile Fe^{2+}, for the control of cell metabolic activities.[33, 34] Likewise, a careful regulation of the relative concentrations of the Fe^{2+} and Fe^{3+} species is necessary for regulating the abundance of reactive oxygen species (ROS) toxic to cell viability, e.g., through the Fenton reaction. Currently, the mainstay of anemia treatment remains on providing additional iron via foodstuffs, as well as for reducing excess metal by iron chelation. It is still an under-explored area that targets iron related diseases through genetic design of enzymes.

2.9 Unknown part about ferritin study

A molecular framework has been established via biochemical and spectroscopic studies.[5, 35] Considering the relative complexity of the ferritin protein, with an approximate radius of 10 nm and the presence of a few thousands of Fe ions in the core, along with the aspect that often the active site is buried deep within (and away from the electrode surface), the interpretation of the electrochemistry is generally not expected to be straightforward. Both three-fold and two-fold channels have been considered for the iron ion pathways, with the specific iron oxidation occurring, in the ferroxidase center[34], located about 0.7 nm from the inside surface of the protein shell and 1.2 nm from the exterior surface[27]. The overall diameter of ferritin is about 12.5 nm.[20] It was indicated, for instance, that oxidant/reductant entry into the ferritin core may not be necessary for the Fe^{2+}/Fe^{3+} redox reactions, based on the evidence that the dynamics continue even in the presence of large molecules, of sizes larger than the typical channel widths of 0.5 nm in the ferritin. However, there is still considerable ambiguity on the mechanisms related

to the Fe^{2+} dynamics out and into a ferritin core. The redox kinetics of ferritin were previously recorded as subject to a variety of factors, ranging from pH and surrounding buffer content[24]. It was seen that the presence of external oxidizing agents, such as $Fe(CN)_6^{3-}$ or Cytochrome c, seem to be as effective as O_2 in promoting Fe^{3+} in the ferritin core. While long-range electron transfer, mediated through electron tunneling through the protein matrix, was advocated for the redox reaction/s at the core, it was also suggested that[36] an "unsuspected electron-transfer process" may be responsible for the Fe^{2+} oxidation, concomitant with the understanding that the ferritin may serve as an electron-storage molecule. Various hypotheses can be made via interaction with other redox pairs or detection of iron releasing; however, there still large ambiguities about the electron path inside ferritin since the direct detection of electron paths in ferritin are still missing.

2.10 An alternative approach is to look for ferritin in other systems

A recent study[2] reported that a long term glow in a marine worm named Chaetopterus[3]. The bioluminescent light is generated in the worm mucus where ferritin is abundant as well as an unexpected high iron level. In Chaetopterus, as long as 12 hours light production[2] in mucus cannot be explained by energy release from a single chemical reaction. The sequence of ChF was initially identified through the 82% similarity to HuHF[2]. The overall structure and near-identical active sites of HuHF and ChF has been confirmed via crystallography. Although great structural similarities have been confirmed, a major challenge is to understand how subtle differences in structure among the ferritins can greatly diversify their functionalities. More specifically, from a dynamic perspective, an 8-fold higher ferroxidase rate[3] of ChF compared to HuHF is yet to be further understood. This charge transfer study provides the insight of dynamics during iron loading that paves way to target the role of specific residues.

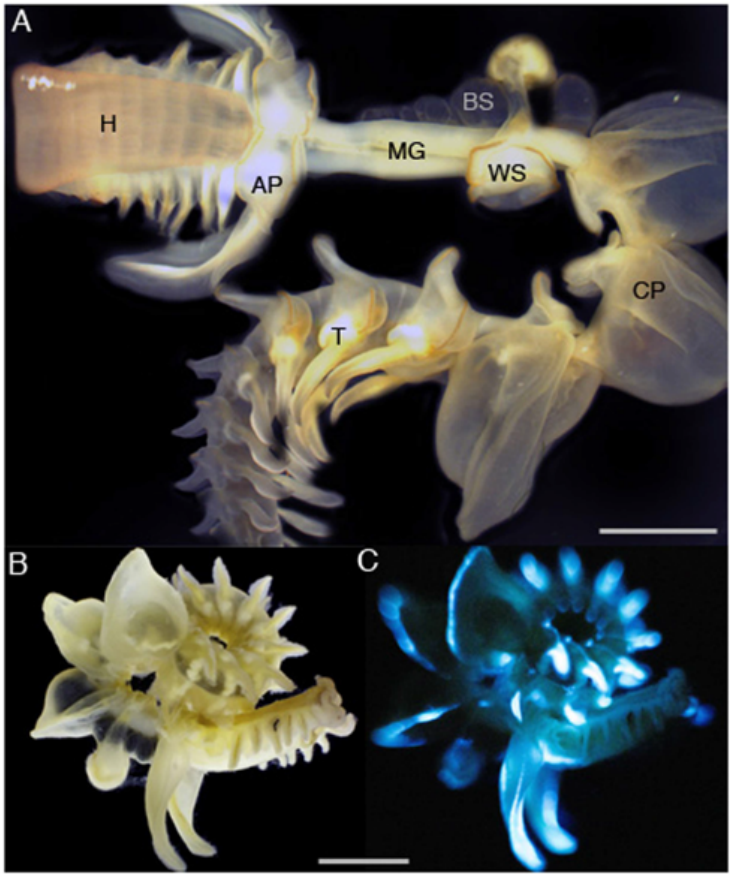

Figure 2.6: An image of a long term glow in a marine worm named Chaetopterus[2]

Chapter 3

Oxygen deficient, nanostructured tungsten oxide for enhanced photoelectrochemical charge transfer and stability

The role of non-stoichiometry in a hierarchically structured WO_{3-x} electrode, constituted from nanoscale fuzziness as well as microscale wire morphology, on the photoelectrochemical response is investigated. Through x-ray photoelectron spectroscopy (XPS) studies, the relative amounts of the various oxidation states of the constituent W are probed with respect to the observed response. It is concluded that an intermediate/optimal number of vacancies, yielding a W^{6+}/ (W^{5+} + W^{4+}) ratio of around 2, would be beneficial for increasing the photocurrent. It is posited that defect engineering combined with optimized band structure modulation could be used for enhanced photocurrent density as well as electrode stability. The work would help considerably elucidate the role of defects as well as charge carriers for oxygen evolution reaction (OER) efficiency increase.

3.1 Introduction

The possibility of incident sunlight passively splitting water[12, 14, 37] to constituent hydrogen and oxygen, through the designed placement of the semiconductor conduction band (CB) and the valence band (VB) with respect to the H_2O/H_2 reduction potential and the H_2O/H_2 oxidation potential, respectively[37], is of immense scientific and technological interest[1]. While the possibility of internal electrochemical potential energy differences to efficiently drive such chemical decomposition reactions could usher in a new paradigm for energy utilization and harness, the technological attraction of such research arises from finding yet another use of solar radiation[38–44]. However, in practice, it has been found necessary to apply voltages[12, 45] in excess of the standard redox potentials (i.e. an overpotential) of the order of 0.1 V (for H_2 production, through the hydrogen evolution reaction, HER: $2H^+ + 2e^- \rightarrow H_2$) and at least 0.4 V (for O_2, through the oxygen evolution reaction, OER: $2H_2O \rightarrow O_2 + 4H^+ + 4e^-$) due to issues related to the activation of disparate intermediate species (e.g., disintegration of adsorbed OOH for oxygen evolution due to intrinsic scaling relations[46], etc.), for the production of the respective gases from the catalyst surface. The limiting kinetics of OER, through the seemingly necessary larger overpotential, then presents a challenge for the overall efficiency of water splitting. Moreover, strongly active intermediates may poison the photoelectrode or react with the electrolyte constituents, which lead to undesired species, e.g. peroxides. Such features are deleterious for highly efficient photocatalysts[47, 48] and stability even at the few hour level. While titanium oxide or hematite based photoanodes have been reported to have higher long-term stability of the order of a thousand hours, intrinsic issues related to a large bandgap and poor conductivity[49], respectively make their usage difficult. Consequently, factors that may reduce the overpotentials, with respect to the detailed physico-chemical features of the catalyst material as well as the underlying implications for the interaction of adsorbed intermediates, need to be examined[50]. Yet another foundational notion involves hole carrier (h^+) transfer to the surface

(whereby the OER proceeds through a reaction of the type: $2H_2O \rightarrow O_2 + 4H^+ + 4e^-$), which implies bond breaking and the consequent instability. However, if there was a mechanism through which the bond deficit at the surface could be compensated, such instability of the surface could presumably be reduced. We hypothesize that oxygen vacancies, with related electron excess, could reduce the deleterious effects due to h^+ at the surface. In this regard, we use WO_{3-x} as a prototype[51] for investigating such effects in photoelectrochemical experiments with application to OER kinetics. The material choice was based on the relatively favorable (i) bandgap (Eg = 2.6 eV[9]) of the parent n-type WO_3 semiconductor to harness visible light, (ii) band alignment, where the WO_3 valence band is much more positive (by 1.6 V) compared to the standard OER potential of 1.2 V, (iii) stability of the oxide to further self-oxidation, e.g., due to the higher O/W ratio compared to say, Cu_2O or Fe_2O_3. In addition to the reasonable Eg, it was previously noted that non-stoichiometric WO_3 could exhibit significant metallic conductivity[52, 53] precluding some of the semiconductor related issues related to obtaining high current densities. Much previous work on stoichiometric WO_3 was focused on morphological considerations[8], and intended to use nanostructuring[54] primarily as a means to increase the surface area to volume ratio, and reduce minority carrier (h^+) diffusion length[11]. Concomitant studies[55] on WO_{3-x} did not pay much attention to the specific role of the extent of non-stoichiometry but focused more on enhancing charge transfer on oxide/electrolyte interface and improving electrical conductivity through doping[11, 56]. For example, oxygen vacancies were introduced as shallow donors into WO_3 using oxygen-deficient atmospheres[10, 11, 56], e.g., through hydrogen annealing. Enhanced photocurrents (close to an order of magnitude larger compared to the stoichiometric compound) combined with photo-stability were proposed and rationalized as due to increased carrier density as well as induced photocatalytic effects, i.e., through a "multi-channel" process[11] involving oxygen vacancy mediated localized surface plasmon resonances as well as valence-/conduction-band transitions, enabling light harvesting over a range of wavelengths (200 nm – 2000 nm). The presence of oxygen vacancies was inferred through x-ray photoelectron spectroscopy (XPS)

studies and a consideration of the peak shifts due to the W^{5+}, cf., the typical W^{6+} in WO_3. The non-stoichiometry was even implicated in diminishing the possible peroxo-species induced dissolution of the oxide[56]. In this chapter, we focus on issues related to the obtaining of maximal and stable photoelectrochemical current density in WO_{3-x} electrodes primarily considering (i) the surface morphology, (ii) non-stoichiometry, and (iii) sensitivity to ambient conditions. Such issues are broadly related to the practical performance of photo-electrode systems, where in addition to suitable band alignment, the facile charge carrier movement to the surface for their interaction with the water as well as interfacial charge transfer kinetics must also be optimized.

3.2 Fuzzy morphology of tungsten induced by He plasma

The initial material was constituted from polycrystalline tungsten discs (2 cm in diameter and 1.5 mm in thickness). After polishing by grit paper, the samples were ultrasonically cleaned in alcohol and acetone. Exposing the sample to low energy and high flux He plasma (5×1018 $cm^{-2}s^{-1}$, with an energy of 60 eV), for 30 minutes and a temperature of 1120 K, generated the fuzzy nanostructure. Under such conditions, the accumulation coupled with the diffusion of He in the vacancies of the tungsten yields the fuzzy structure. The He plasma was generated in the Pisces-A chamber, that produces a He ion flux (from an arc discharge[57, 58]). The samples were then taken out of the chamber and subject to oxidation under pure O_2 under different conditions, so as to vary the WO_3/WO_{3-x} ratio, as follows: (i) For the S1 sample, oxidation at 22 mTorr at 700°C for 30 minutes. (ii) For the S2 sample, oxidation at 5 Torr at 500°C for 30 minutes, followed by annealing at 500°C for 3 hours in air. (iii) For the S3 sample, oxidation at 5 Torr at 500°C for 30 minutes, followed by annealing at 500°C for 9 hours in air. A reference W sample (without plasma processing) was treated in similar conditions to the S2 sample. It was previously noted31 that the activation energy for the oxygen vacancy formation decreases with reducing oxygen partial pressure and consequently annealing in air was preferred over annealing in pure

oxygen, for modulating the stoichiometry.

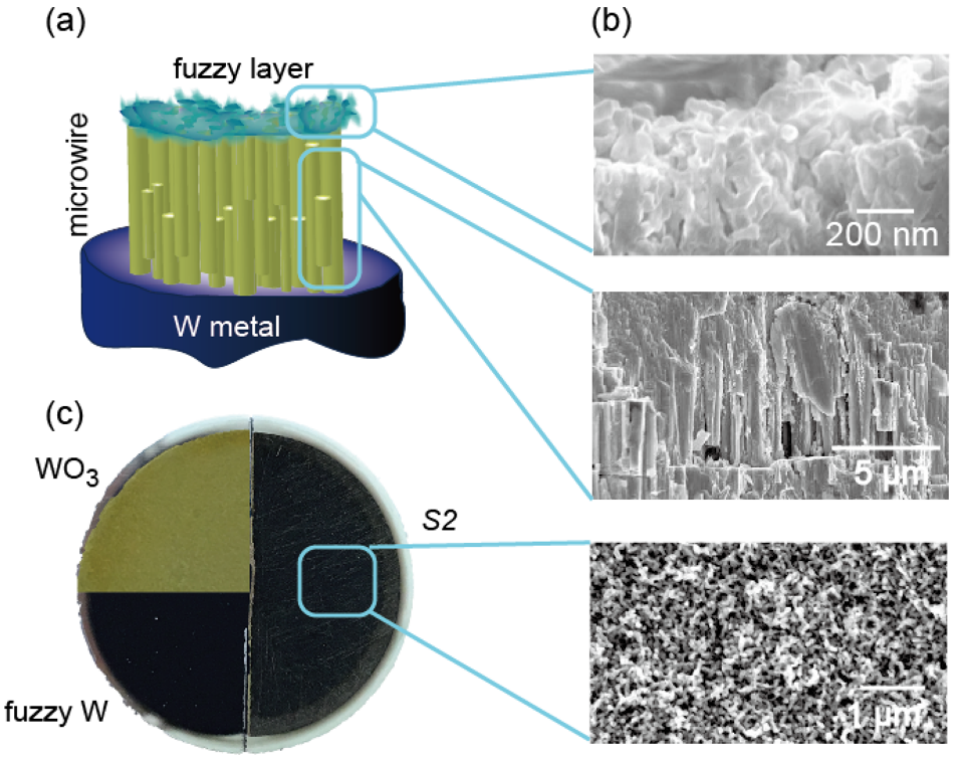

Figure 3.1: (a) Schematic cross-section of hierarchical layer structure of tungsten oxide samples, comprised of a large surface area nanoscale "fuzzy" and microscale wire tungsten oxide layers interfaced to a tungsten (W) metal substrate electrode, (b) SEM images of the cross-section of a sample (S2) with WO_3/WO_{3-x} ratio of 2. (c) Optical micrograph images of a reference WO_3 – without nanostructural features (top left), hierarchical WO_3 constituted from the fuzzy nanostructure (bottom left), and WO_{3-x} (right) samples.

A unique fuzzy surface morphology[57–60] was first induced through helium plasma bombardment of metallic W substrates: Figure 1. On further oxidation, a micro-wire like morphology (spanning a length of 8 μm) was observed below the fuzzy layer[61] at about 200 nm from the surface. The microwires are formed through the subsequent oxidation of the fuzzy layer covered W. While the detailed mechanism is yet to be determined, the channeling of the oxygen through pores in the fuzzy layer, and the consequent differential oxidation rate between the fuzzy tungsten and underlying crystalline tungsten may be responsible, for the microwire morphology.

Scanning electron microscopy (SEM) images, indicating the morphology of the other tested samples, i.e., S1 and S3, in addition to that of sample S2 – depicted in Fig.3.1(b)

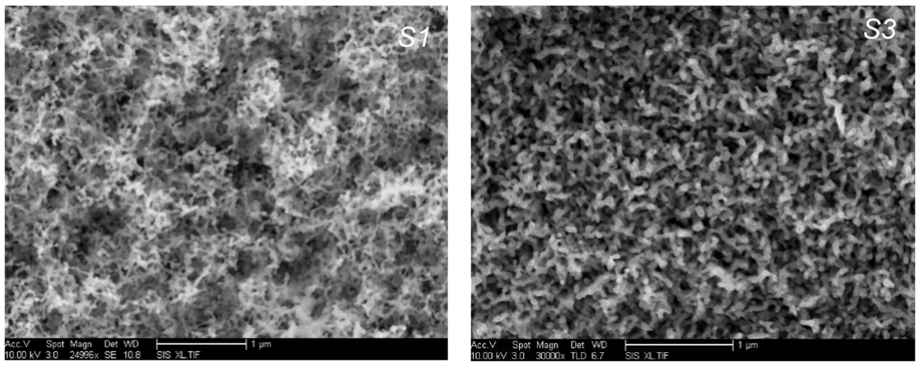

Figure 3.2: SEM images of samples S1 and S3.

The fuzzy nanostructured surface[62] yields a blackish appearance, implying at the very outset a greater visible light absorption[63]. In addition to the large surface area[64], the spatial extent of this morphology is much higher than the optical penetration depth (δ) for visible light: from Eqn. (a). The micro-wire like layer, reported here for the first time, may also be of advantage in that it may provide carrier channels to/from the fuzzy layer via the underlying W metal enabling facile electrical carrier transit[48], from photon conversion. To study the role of non-stoichiometry in WO_{3-x} we varied x through changing the thermal oxidation conditions on the fuzzy tungsten sample.

3.3 XPS structural characterization

X-ray photoelectron spectroscopy (XPS): The XPS spectra were measured at the UC Irvine Materials Research Institute (IMRI) with Kratos AXIS Supra. To eliminate the influence of carbon inside porous structure, we deployed Ar^+ sputtering for all the samples. X-ray diffraction (XRD): The XRD patterns from a Rigaku MiniFlex system were measured in reflection mode using Cu Kα (λ = 0.15406nm) radiation at 40kV and 40mA with a scan rate of 1° per 30s.

Scanning electron microscopy (SEM) was performed on the FEI XL30 SFEG UHE SEM.

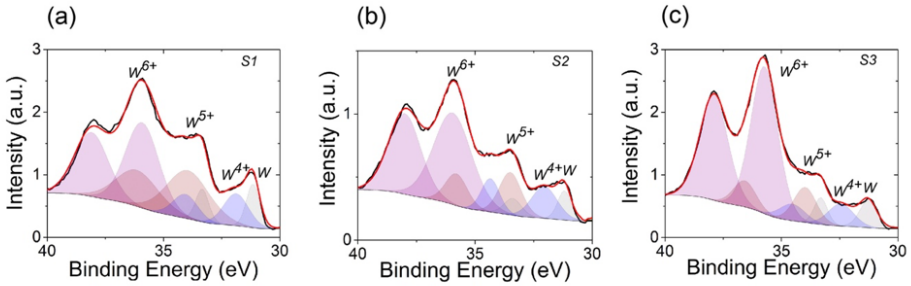

Figure 3.3: X-ray photoelectron spectroscopy (XPS) based spectra of the WO_{3-x} samples, (a) S1, (b) S2, and (c) S3 with varying x. The "N " in SN refers to the WO_3 / WO_{3-x} ratio. The number of oxygen vacancies in the tungsten oxide samples decreases in the order S1 > S2 > S3.

X-ray photoelectron spectroscopy (XPS) and x-ray diffraction (XRD) were used for detailed structural characterization of the samples, processed to various extents of oxidation. However, due to (a) the complexity of WO_{3-x} crystal structure (monoclinic), (b) the relatively small stoichiometric variations due to oxidation, and (c) the frequent occurrence of a mixture of phases corresponding to varying oxygen vacancy content, as was also the case in previous studies[10, 11] – as also indicated in Section B of the Supporting Information. XRD characterization was hence found to be less useful compared to XPS. We characterized quantitatively the extent of non-stoichiometric influence, correlated to the net oxidation state of the WO_{3-x} material, through the following ratio:

$$\mathrm{N} = \frac{WO_3}{WO_{3-x}} = \frac{W^{6+}}{W^{4+}+W^{5+}}$$

The obtained XPS spectra were deconvoluted to fit the oxidation states of the tungsten in the WO_{3-x}, i.e., W^{6+}, W^{5+}, and W^{4+}, as indicated in Figure 3.3. We present the results from three representative samples, reporting a parameter: SN, where N is the numerical value of the ratio of WO_3/WO_{3-x}, for three values of N. The characterization of S1, S2, and S3, with a steadily decreasing number of oxygen vacancies, then yields substantial insight. While alternate methods such as XAFS (x-ray absorption fine structure) and ESR (electron spin resonance) techniques

may be useful in further understanding, e.g., through examining local structure in terms of W-O coordination, trapping of electrons at oxygen vacancies[65, 66], etc., our aim was to specifically focus on the oxidation state of the W.

3.4 Photoelectrochemical characterization of fuzzy tungsten

A variety of electrochemical techniques, incorporating potentiostatic methods, e.g., linear sweep voltammetry (LSV) cyclic voltammetry (CV), frequency based techniques – such as electrochemical impedance spectroscopy (EIS) were employed for a detailed characterization of the OER capability of the WO_{3-x} samples. A three-electrode setup, with the samples as the photoanodes, Pt foil as the counter-electrode and Hg/Hg_2SO_4 as the reference electrode was deployed. The measurements were performed via potentiostat VersaSTAT3 (with IR correction). The photoresponse were measured under simulated sunlight generated with a 300W Xenon lamp (Newport 66483) coupled with an AM 1.5 global filter (Newport 81094). All linear sweep voltammograms and cyclic voltammograms were collected at a scan rate of 20 mV/s. Electrochemical impedance spectroscopy (EIS) was operated at a frequency range from 100 kHz to 100 mHz with 10mV perturbation at different potentials.

A variety of electrochemical techniques, incorporating potentiostatic methods, e.g., linear sweep voltammetry (LSV), cyclic voltammetry (CV), as well as frequency based impedance measurements – such as electrochemical impedance spectroscopy (EIS) - see Experimental Section for details, were employed for a detailed characterization of the WO_{3-x} sample performance in photoelectrochemical processes. We first indicate the results of an LSV scan on individual samples of S1, S2, and S3. The photoresponse was measured under simulated sunlight generated with a 300 W Xenon lamp coupled with an AM 1.5 global filter - see Experimental Section for more detail. The samples were configured as the working electrode in a three-electrode setup, and tested in a 0.1 M K_2SO_4 (pH = 7) background electrolyte: Figure 3.4 (a). In the

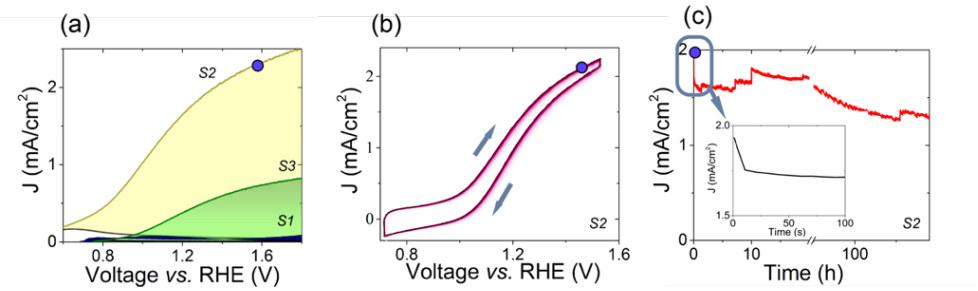

Figure 3.4: Photocurrent, in linear sweep voltammetry (LSV) of samples S1, S2 and S3 in 0.1M K_2SO_4, the blue dot indicates the current density @ 1. 56 V_{RHE}. (b) Cyclic voltammetry (CV) based characterization of sample S2 over ten cycles indicates behavior characteristic of nano-/micro-scale electrodes, due to hierarchical electrode sub-structure as well as charge storage proportional to the area enclosed between the forward and reverse voltage scans, (c) OER related photocurrent stability test (@1.56 V vs. RHE) of S2 for the first twenty hours and subsequently extended another ninety hours. The inset indicates an expected current decay over the first few seconds due to Cottrell diffusion limitations.

anodic (increasingly positive voltage, reckoned with respect to the reversible hydrogen electrode: RHE) scan, it was noted that the oxidation current density was the largest for the sample with the intermediate number of oxygen vacancies, i.e., for sample S2 (2.3 mA/cm^2 @1.56 V_{RHE}) compared with sample S1 (0.05 mA/cm^2 @1.56 V_{RHE}) constituted from more vacancies, or Sample S3 (0.7 mA/cm^2 @1.56 V_{RHE}) with a smaller number of oxygen vacancies. The area normalization for computing the current density was done through considering the geometric projected area (0.375 cm^2) of the samples. Further characterization of the current density (J) as a function of the voltage (V) - with a voltage scan rate: v, of 20 mV/s, as shown in Figure 3.4(b), indicated a pronounced hysteretic behavior only for sample S2, indicative of charge storage and parameterized by the difference between the forward and reverse scans. Note that the depicted J – V curve may be considered equivalent to a capacitance (C)-voltage (V) curve, which may be inferred by multiplying the J by the constant area (0.375 cm^2) and dividing by the constant voltage scan rate (= dV/dt). The area enclosed in the J-V or the C-V curve is related to the total stored charge. The related J-V curves for samples S1 and S3 have been included in Section D of the Supporting Information. It was noted that the cathodic current density was smaller compared to the anodic current density. We interpret the current density variation in terms of the

h^+ facilitating the extent of water oxidation, as a positively (/negatively) increasing voltage on the WO_{3-x} samples induces upward (/downward) band bending near the surface causing hole accumulation (/depletion) and an increased (/decreased) current density. Moreover, the general shape of the CV curve seems to indicate a tendency towards convergent diffusion (also termed a steady-state variation[67]), where the diffusion time scale (r^2/D) is short compared to the time involved (Fv/RT) in obtaining the voltammogram). The micro-/nano-scale characteristic of the sample is manifested through the length scale of r with electrolyte species diffusion coefficient: D, of 10^{-5} cm^2/s in K_2SO_4 or H_2SO_4[68, 69]). The F is the Faraday constant (96,500 C/mol), R is the gas constant (= 8.3 J/mol·K), and the experiments were performed at room temperature (T 300 K). Considering the small r, it is plausible that the nanoscale fuzziness as well as the microscale wire morphology related to the hierarchical structure of the WO_{3-x} electrodes are involved in the electrochemical interactions. As such small length scales would nominally imply smaller capacitance[67] and lower charge storage, it is plausible that alternative charges, e.g., oxygen vacancies, may be involved[70]. We observed that the photoelectrochemical current density (1.7 mA/cm^2 at a voltage of 1.56 V_{RHE}) was relatively stable48 over a time period of more than 110 hours: Figure 3.4(c) – and is among the highest reported value to date for tungsten oxides[10, 48]. The inset in Figure 3.4(c), indicates an expected current decay over the first few seconds due to Cottrell diffusion limitations[67]. The subsequent variation in the current may be indicative of kinetic processes related to oxygen vacancy diffusion, bubble and adsorbate formation, change in surface characteristics.

3.5 Impedance Characterization of non-stoichiometric fuzzy tungsten

To obtain a better understanding of the kinetics, impedance spectroscopy (EIS) was performed on the WO_{3-x} samples, over a range of frequencies (100 mHz to 100 kHz): Fig. 3.5(a),

and the obtained spectra modeled in terms of a Randles equivalent circuit, depicted in the inset to Fig. 3.5(b). We adopt such a relatively simple model for obtaining the equivalent series resistance (ESR): R_s, the charge transfer resistance: R_{ct}, and the concomitant equivalent capacitance: C. While more elaborate representations are possible and have been done, they essentially devolve into the Randles circuit form[7]. The obtained Rct may be parameterized in terms of the exchange current[71] (i_o) - through $R_{ct} = RT/Fi_o$, and may be considered proportional to the rate at which the water oxidation occurs, and may consequently be adopted as one metric of the OER efficiency, i.e., a lower Rct would imply more facile hole carrier transport to the surface and enhanced efficiency. An ESR of 10 Ω was observed from the high frequency part of the EIS spectrum. The R_{ct} and the C was estimated from the EIS (carried out with the samples in both dark and simulated sunlight illuminated conditions) fits and are plotted as a function of the voltage in Figures 3.5(b): dark, (d): illuminated and (c): dark and illuminated, respectively. It was noted that a peak was observed in the R_{ct} for all the samples with the lowest peak value obtained for S2. Of the studied samples, S1 and S3 have maximum and minimum oxygen vacancies, respectively and were observed to have a higher R_{ct} compared to S2. The R_{ct} peak may be related to the potential at which the OER tendency is minimal (smallest i_o) with the physical implication that the available h^+ for water oxidation is significantly reduced at such a voltage. These results will be discussed later, with respect to band structure modulation, in the context of Figure 3.7. The related EIS curves for samples S1 and S3 have been included in Figure 3.6.

It was also observed that the C decreased monotonically with the applied potential (in the dark as well as under illumination), with the largest value for S2. The C was previously considered[71] in terms of the combination of a trap based surface state capacitance (Css: related to h^+ trapped in oxygen vacancies), which varied inversely with the R_{ct}, i.e., a minimum in the Css was correspondent to a maximum in the R_{ct} and vice versa. However, in our study we do not see such an inverse correspondence between the Css (as related to C) and the R_{ct}. While the charge stored in S2 is larger than in S1 and S3, as also inferred through the area under the

respective current density-voltage curves: Figure 3.4(b), oxygen vacancies do not seem to be the sole reason, as the quantity of vacancies decreases in the order S1 > S2 > S3. Consequently, there seems to be an alternative charge storage mechanism in S2.

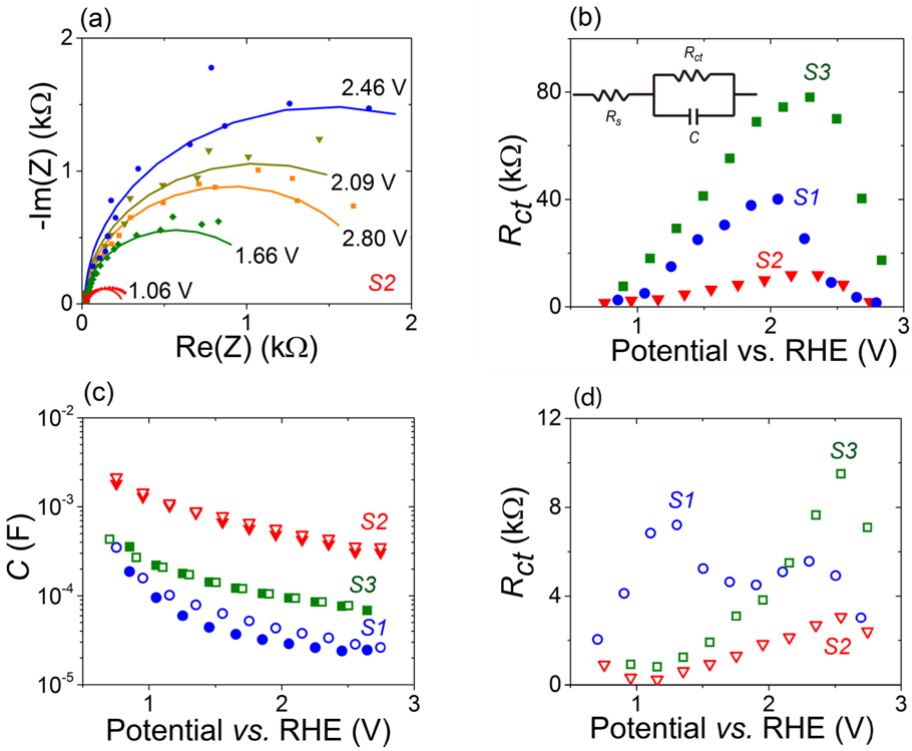

Figure 3.5: (a) A Nyquist plot indicating the negative of the imaginary: -Im (Z) and Re(Z) components of the impedance for sample S2, at various applied voltages (with respect to RHE). (b) The variation in the charge transfer resistance (R_{ct}) of S2 (in the dark) with applied voltage indicates a peak at which the exchange current density for OER is minimal. In addition to R_{ct}, the equivalent series resistance: Rs, and the concomitant equivalent capacitance: C, were extracted through fitting the Nyquist plots to a Randles circuit model – inset. (c) A steadily decreasing capacitance with respect to the voltage for S2 in both dark (solid symbols) and illuminated (unfilled symbols) conditions, (d) A peak, shifted in voltage with respect to the dark condition in (b) was observed in the R_{ct} for S2 on illumination.

3.6 Characterizing the optical response and carrier concentration

We characterized the optical penetration depth (δ) for the sample, from the relation[72]:

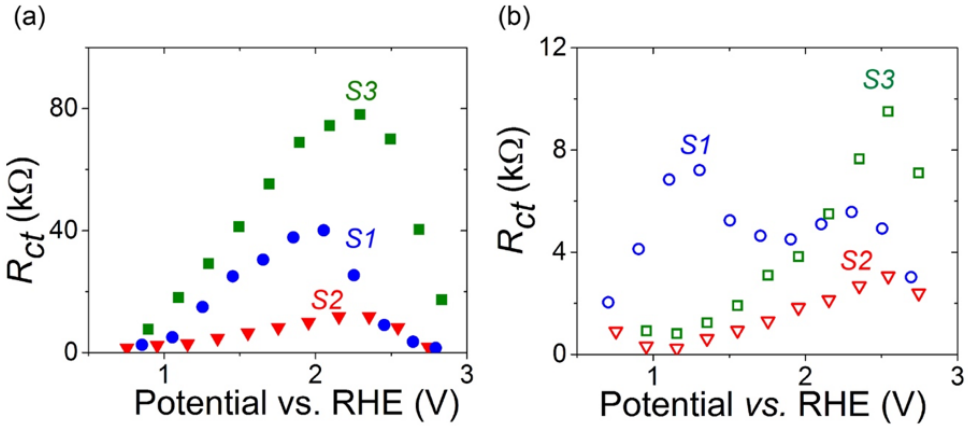

Figure 3.6: (a) R_{ct} vs. V (dark) (b) R_{ct} vs. V (under illumination) in K_2SO_4

$$\delta = \frac{1}{\sqrt{\pi\mu\sigma f}} \text{ (a)}$$

In the above equation, μ is the magnetic permeability equals to $4\pi \times 10^{-7}$ H/m[73], σ is the electrical conductivity f is the frequency of the incident electromagnetic radiation. For the tungsten oxide samples, we used σ: 1.76 S/m[52], and f of 6.3×10^{14} Hz, corresponding to a wavelength of 476 nm to obtain a δ of the order of 1.5 μm.

The hole carrier density (Nh) was estimated from the relation[74]:

$$N_h = \frac{2\varepsilon\Delta V}{eL_h^2} \text{ (b)}$$

Here, $\varepsilon = \varepsilon_0 \times \varepsilon_r = 8.854 \times 10^{-12}$ F/m is the net permittivity with ε_r being the relative dielectric permittivity[11] of 20 for the WO_{3-x}, Δ V is the band bending, e is the elementary unit of electronic charge (= 1.6×10^{-19} C) and L_h is the hole diffusion length.

We hypothesize that excess h^+ may provide the means for such charge storage. At the very outset, the introduction of oxygen vacancies (V_o), functioning as electron donors[75], in WO_{3-x} would induce an intrinsic upwards band bending at the surface[76], causing h^+ accumulation at the surface: Figure 3.7(a). This figure indicates the nominal band bending expected at equilibrium in n-type WO_3 where the Fermi energy (E_F) would be aligned with the OER potential. We used previously determined values[77] for locating the oxygen vacancy (V_o) level. Under the application of a positive (/anodic) potential on the semiconductor, the conduction band (CB)

and the valence bands (VB) shift down: Figure 3.7(b). This figure also indicates that under illumination the band bending would be reduced due to e^- h^+ pair excitation. In one viewpoint, the band positions in Fig. 3.7(c): dark, and (d): illuminated, refer to situations corresponding to diminished h^+ concentrations, hence diminishing the exchange current (i_o) related to the OER and leading to a maximum in the R_{ct}. The reason for such diminished h^+ concentration is that when the CB in the bulk is depressed, due to the application of voltage, up to the position of the VB at the surface, the e^- in the CB interact/recombine with the h^+ in the VB yielding diminished h^+ concentration and i_o. Under illumination, band positions where the h^+ are compensated by the e^- are shifted 0.4 V due to the additional photovoltage (Vph): Fig. 3.7(d). The positions of the R_{ct} peak, observed at 2.3 V (sample in the dark) and at 2.7 V (sample illuminated) in Figures 3.5(b) and (d), may be related to such band modulation. For instance, the peak itself may correspond to a minimal carrier concentration (i.e., the CB being low enough that the e^- would compensate for the h^+ at the surface from the VB) and a minimal i_o. The diminishing of the R_{ct} before and after the peak, is indicative of enhanced kinetics and i_o, and would be due to excess electrons and holes at the surface, respectively. We also speculate that the additional peak in S1: as observed in Figure 3.5(d) at 1 V, may be attributed to the oxygen vacancy levels, which may serve for a recombination site for photo-generated charge carriers. The recombination reduces the exchange current (i_o) and leads to a peak in the R_{ct}. The peak was not observed in S2 and S3, as the concentration/number of oxygen vacancies is reduced in these samples. As previously noted, a critical oxygen vacancy concentration/non-stoichiometry, as in S2, seems to be necessary for enhanced photoelectrical current and optimal OER performance. We then surmise that too small (/large) a h^+ concentration - as in samples S3 (/S1) - implies a reduced OER capability, i.e., due to inadequate number of carriers and the relatively small area over which h^+ could aggregate, respectively. Consequently, a design for a reasonably wide depletion length at the surface over which the h^+ would accumulate may be considered an objective. It may be estimated from Eqn. (b) in this Section, that a magnitude of the band bending (ΔV)

of 2.3 V, i.e., corresponding to the R_{ct} in Figure 3.5(b), may be obtained with an N_h of 2 $\times$ 1017 cm^{-3}, a hole diffusion length (L_h) of 150 nm[48]. Such a magnitude of the voltage would effectively span the tungsten oxide band gap, and place the top of the VB at the sample surface close to the energy level of the oxygen vacancies. Consequently, at applied voltage less (/greater) than 2.3 V, there would be more (/less) electrons compared to holes, and at 2.3 V, the e-h compensation leads to a low current and a large R_{ct}. We also note that given an intrinsic carrier concentration (n_i) of $10^{-}3$ $cm^{-}3$ (from an E_g 2.6 eV) and an electron concentration (n) 1015 $cm^{-}3$ corresponding to the electrical conductivity[53] of the tested samples, we obtain from the relation: $np = ni^2 \exp(e\delta V/kBT)$ a hole carrier concentration (p) of the order of 1017 $cm^{-}3$ with such a δV, implying that our formulations are reasonably self-consistent. One tool in enhancing the efficiency may then be through engineering the band bending which is enhanced in the presence of defects, such as oxygen vacancies and related non-stoichiometry, and which may be modulated through annealing in various oxygen partial pressures31. Such band bending could provide, at the very outset, a driving force for h^+ accumulation at the surface to facilitate OER. However, it is imperative that the kinetics of the oxidation, through hole interaction with water be considered as well. While some such aspects have previously been applied to evaluating the efficacy of hematite-based electrodes for OER, modeling the oxidation due to h+ from either (i) surface state traps, or (ii) directly from the valence band52, a maximum in the capacitance was observed at energies that may correspond to the surface traps. However, we indicate that such maxima are to be avoided, as they lead to the necessity of precise energy level alignment and the possibility of Fermi level pinning, which would limit and saturate OER activity[49]. Instead, we posit that the electrons from the oxygen vacancies in oxide based photoanodes, which could migrate to the surface[78, 79] be used to partially compensate for the introduced h^+ at the surface, yielding a degree of control over the stability[80, 81] of the surface. The band bending would then need to be designed such that the top of the VB near the surface would be close to the energy level position of the electronic energy levels arising from the oxygen vacancies. Consequently,

an optimal number of h^+ with respect to oxygen vacancies as in S2 could be responsible for the increased photocurrent: Figure 3.4(a), and the enhanced stability: Figure 3.4(c). Lower values are obtained for both an increased number of oxygen vacancies (as in S1) and a decreased number (as in S3). In the case of S1, the quenching of the h+ by the electrons from the vacancies may be responsible for yielding negligible photocurrent, while in the case of S3, the pinning of the Fermi level at vacancy or surface states causes a finite and saturating photocurrent. The large h^+ accumulation in S2 compared to S1 and S3 also results in a larger capacitance and lower resistance (R_{ct}) peak for S2, as in Figure 3.4. While the R_{ct} variation with voltage may indicate the overall distribution of photocurrent contributing defects in the WO_{3-x} band gap, much more detailed investigation is necessary to establish such structural aspects on a firm basis.

3.7 Conclusion

In summary, we have indicated the crucial role of non-stoichiometry in oxides for enhanced photoelectrochemical current density, using WO_{3-x} as a prototype. Given that OER proceeds through the interaction of hole charge carriers (h^+) with water and that the presence of h+ implies surface instability, we indicate that a charge compensating mechanism through electrons from oxygen vacancies[82] may be beneficial. Indeed, we found that a critical vacancy and h^+ concentration, as in sale S2, increases the photoelectrochemical performance. The accumulation of h^+ at the surface over a distance of the diffusion length to accomplish band bending for enhanced kinetics is also posited. It is hoped that the consideration of such defect engineering[65, 66] aspects, perhaps at the atomic level[13], would be helpful in designing higher efficiency electrodes for water oxidation[66].

3.8 Acknowledgement

This chapter has been published on Journal of Materials Chemistry A in 2017, ”Hierarchically structured, oxygen deficient, tungsten oxide morphologies for enhanced photoelectrochemical charge transfer and stability.”, by Chen, P., M. Baldwin, and P. R. Bandaru.The authors are grateful for support from the Defense Advanced Research Projects Agency (DARPA: W911NF-15-2-0122) and the National Science Foundation (NSF: CBET 1606192 and CMMI 1246800). The discussions with H. Yamada, R. Narayanan, and E. Martinez are appreciated.

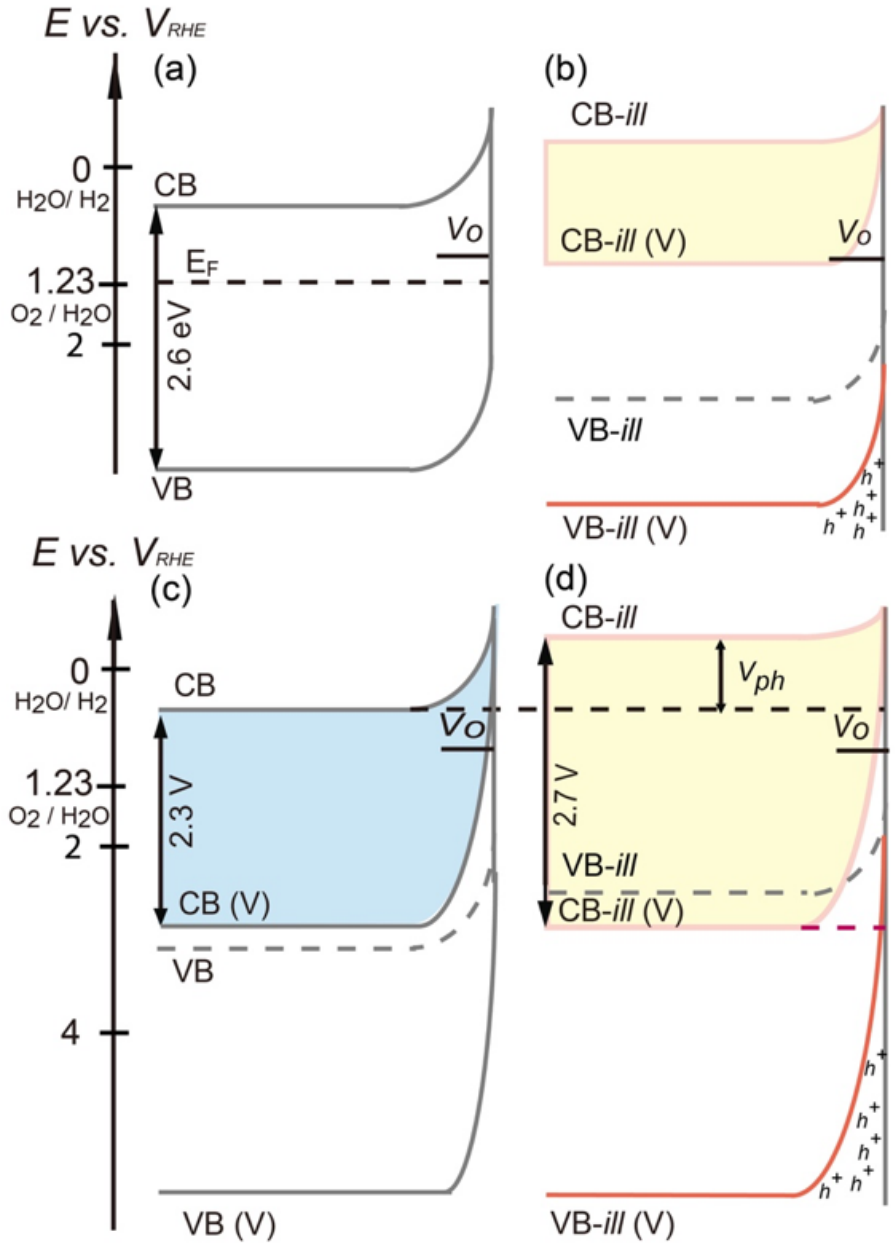

Figure 3.7: (a) Schematic band structure (CB: conduction band and VB: valence band) diagram of WO_{3-x} interfaced with a K_2SO_4 electrolyte, and voltage/energy levels considered with respect to the reversible hydrogen electrode (RHE). The bandgap of 2.6 eV along with the oxygen vacancies (V_o) are indicated. (b) Under illumination, the photo-generated charges reduce the band bending, implying an upward band shift (i.e., CB-ill and VB-ill) compared to (a). Under application of a positive bias voltage (V), the CB and VB move downwards (i.e., CB-ill (V) and VB-ill (V)), with respect to the original band positions indicated in (a), (c) The band positions at the voltage of 2.3 V corresponding to the R_{ct} peak of Figure 4(b), (d) The band positions at the voltage of 2.7 V corresponding to the R_{ct} peak of Figure 4(d). A critical oxygen vacancy and h^+ concentration at the surface, as in S2, has been found to be necessary for enhanced photoelectrochemical current density. The V_{ph} refers to the photovoltage.

Chapter 4

Static and dynamic charging characteristics of nanoscale fuzzy tungsten surfaces

It is shown that a substantial surface potential and surface charge density modulation may be achieved through He ion bombardment of metal surfaces. Comparing the characteristics of metal W and plasma-irradiated W, it is indicated that a variation of the charge density as well as a more facile kinetic response may be obtained in the latter. The influence of the fuzzy nanostructured morphology in the irradiated W in facilitating such characteristics is quantified through the hydrophobicity and electrochemical analyses. The work has implications to energy storage and transduction via greatly improved kinetics as well as charge transfer efficiency.

4.1 Introduction

The utility of metallic materials, e.g., as electrodes in energy storage, is dependent on the surface charge characteristics. For instance, the degree of electrode polarization – voltage

drop due to development of double layers[83], which determines the electrical capacitance, as well as the electrode kinetics[84], is crucially dependent on the metal as well as the surface type. This leads then to the characterization of the electrode-ambient (e.g., electrolyte) interface as typical of a capacitor or a resistor, as in the case of Pt or Ag/AgCl electrodes commonly used in the laboratory. Probing further into the type and magnitude of the surface charge density (σ), one needs to consider correlations to the surface energy (γ) of the atomic planes[85] interfacing with the electrolyte. For example, in the case of Pt, the σ_s for the (110) at 2.0 J/m^2 is twice that for the (100) plane at 1.0 J/m^2. However, considering their relative number and orientation, as in the case of polycrystalline electrodes leads to an averaging[24] of the σ_s. It is then plausible that either (a) modification of the σ_s while retaining the intrinsic character of the metal, or (b) a partitioning of the surface, which could lead to a different type of averaging, and could be used to modulate resultant surface charging attributes. Ion bombardment can rearrange the crystalline structure and alter the electrochemical performance of the material.[86, 87] In this work, we indicate that ion bombardment of metal surfaces could modify the surface charging properties, whereby both the intrinsic charging character of metal surfaces as well as the surface energy may be altered. We compare, specifically, the characteristics of metal W and plasma-irradiated W in this work. There has been significant amount of research[88] on tungsten ranging from photoelectrolysis[89] of water and photochromism[90–92] to the recycling of W[93–95]. The interaction of very light elements (such as hydrogen and helium) plasmas, with a wide variety of metals ranging from low atomic weights (e.g., Ti, Fe) to higher atomic weights (e.g., W, Mo), has been shown to induce unique surface morphology, i.e., a high porosity, nanometer scale, fuzzy structure: Figure 4.1. Such fuzz formation was first discovered[96, 97] on tungsten material surfaces. The fuzz may be produced on bulk metal surfaces exposed to approximately one third the melting point temperature[86] to a sufficient helium fluence of energy to penetrate the surface. To date, W has been researched most widely to produce the fuzz. Figure 4.1 (b) shows examples of fuzzy surface layer material, which is typically evident as a conglomeration of interconnected

nano-branches of individual thickness down to a few tens of nm. The lengths and geometries of the nanostructures or tendrils are variable, depending of the formation process parameters such as temperature and ion energy, with length scales from sub-micron up to mm in scale. The strong insolubility of He in metals, coupled with energetic implantation, followed by precipitation and mixing of the near surface material, leads to a variety of formed surface structures. Under electron microscopy examination, nanoscopic He bubbles are noted, and were assumed to play an important role in the fuzz formation[98]. The incorporation of He would be expected to impact

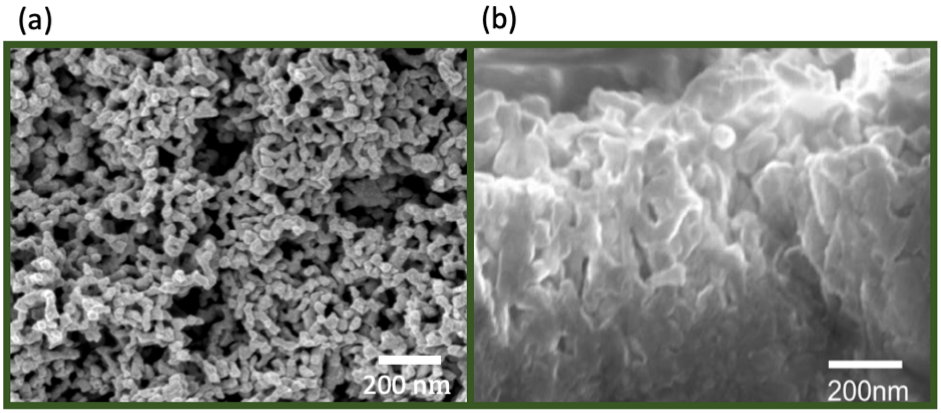

Figure 4.1: SEM images of the fuzzy surface structure. SEM (Scanning Electron Microscopy) images of (a) the surface, and (b) cross-section of the He plasma induced morphology.

the local stress state of the surface, e.g., through atomic unit cell level distortions, and influence the surface tension and related surface charging properties.

4.2 Charge transfer characteristics of fuzzy W

A great insight of charging transfer was obtained through chronocoulometry (CC), where the experimental data for metallic and fuzzy W are plotted in Figure 4.2. Such data may be modeled through considering the Cottrell relation for the net charge accumulation (Q), i.e., $Q = (2nFAC\sqrt{Dt})/\sqrt{\pi} + Q_c$, where C and D are the concentration and diffusion coefficients of the reactants, A is the active electrode area, n is the number of electrons involved in a reaction, and F

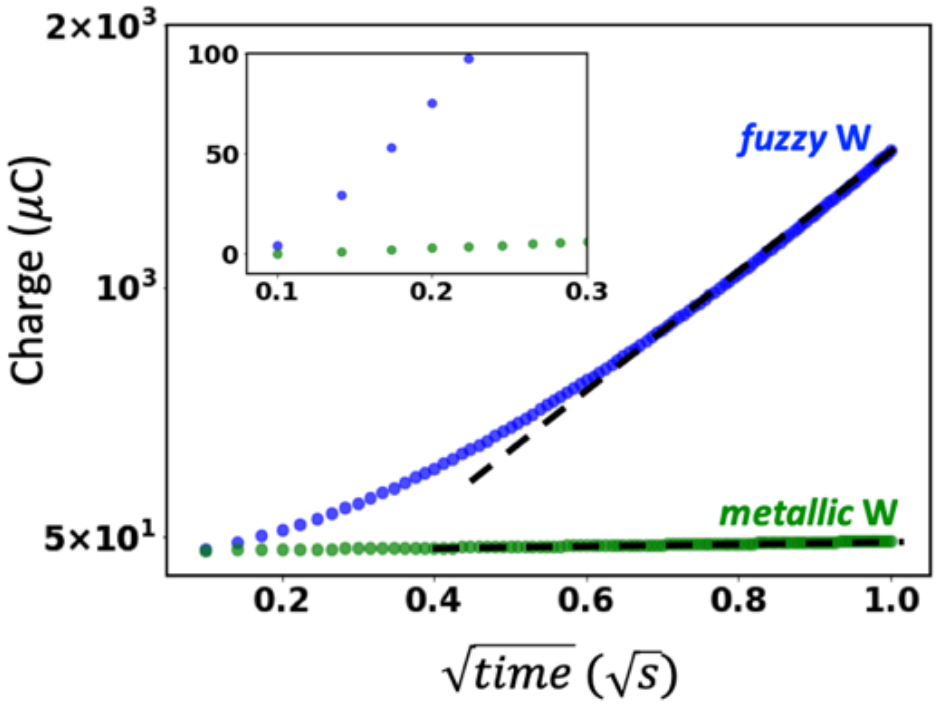

Figure 4.2: Charge transfer characteristics of fuzzy W (in blue) and metallic W (in green) based electrodes with ferrocyanide probed through chronocoulometry (CC). Current is plotted as a function of square root of time. 10 mM $K_4Fe(CN)_6$ in 0.1 M KCl (aq.) was used as the electrolyte.

is the Faraday constant. The first term in the relation indicates the faradic current in response to the applied potential and limited by semi-infinite linear diffusion; Q_c is the charge consumed by the electrode-electrolyte double layer during potential change, and the absorbed charge. The plotted slopes are 2.19×10^{-3} and 3.00×10^{-5} As $^{1/2}$ for fuzzy tungsten and metallic tungsten with R square value 0.999, respectively. The intercepts are 6.79×10^{-4} C and 1.39×10^{-5} C for fuzzy and metallic tungsten, respectively, corresponding to the charge accumulation on the surface. With the diffusion coefficient of ferrocyanide 6.86×10^{-10} m^2/s and Faradic constant is 96485.332 C/ mol, the calculated active area based on Cottrell equations are 0.757 cm^2 and 0.0156 cm^2 for fuzzy and metallic tungsten respectively.

It was noted that at short time, the depletion of the redox species is rapid, then followed by a diffusion limited Cottrell response at longer time scale. For analysis, the range of time was

selected under the diffusion limited regime[99] from 0.3 to 1 second in our case. The electrochemical activity was calculated by dividing electrochemical surface area by the projected area. The active areas are 0.757 cm^2 and 0.0156 cm^2 for fuzzy and metallic tungsten, corresponding to the projected areas 0.2319 cm^2 and 0.1798 cm^2, respectively. The ratio of electrochemical active area for fuzzy tungsten is 3.26, while the value for metallic tungsten is 0.0867. It indicated the intrinsic tungsten has a quite inefficient charge transfer property and may be attributed to the self-dissociation. In contrast, the active area of fuzzy tungsten is 37.7 times higher than metallic tungsten. Therefore, the charge transfer efficiency, a metric of the charge transferred from electrode to reactant – ferrocyanide for our case, is greatly enhanced via fuzzy morphology and surface stability.

4.3 Surface energy study through contact angle measurement

The charge transfer property and electrochemical active surface area have been investigated via chronocoulometry. Aimed at separating the contributions of roughness and surface property of fuzzy tungsten, a relatively quick methodology to assess the modulation of the surface charge σs and the related surface energy aspect is to measure the wetting characteristics of liquid on the solid substrate surfaces. According to the Young equation: $\gamma_S A - \gamma_L A \cos\theta = 0$ (1), with $\gamma_S G$, $\gamma_S L$, $\gamma_L G$ as the substrate-air, substrate-liquid and liquid-air interface energies, respectively, and θ is the substrate-liquid contact angle. Moreover, an increase θ (decreased wetting) is indicative of the reduced polarizability of the surface[100]. The related contact angle measurements on the (i) fuzzy W, and (ii) metallic W surfaces are indicated in Figure 4.3 (a). The θ of metallic W was in the range of 60° to 80° and broadly spread over a large pH range in distinct contrast to the observations on fuzzy W with a more peaked variation in the range of 10° to 65°. However, Young's equation works on ideal surface, to take the roughness into consideration, the Wenzel's equation is applicable to modify the contact angle. Wenzel's equation:

$$\cos\theta_w = r\cos\theta_m$$

θ_m is the measured contact angle, θ_w is the modified contact angle for rough surface and r refers to the roughness that we got via electrochemical active area over projected area is 3.26 from previous session. Suggested by Wenzel's equation that for the case θ_m ¡ $\pi/2$, introduction of roughness will enhance the tendency for liquid to wet further and on the other hand when $\theta_m > \pi/2$ the de-wetting tendency will be enhanced.

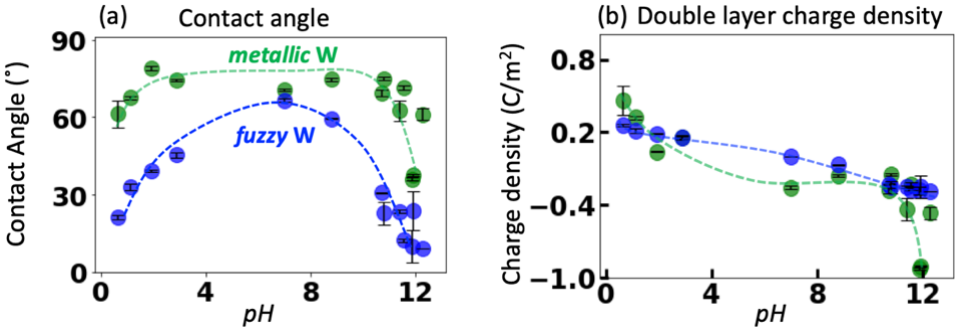

Figure 4.3: The variation of the contact angle (θ) and surface charge density (σs) as a function of pH, for (a) and (b): fuzzy W was plotted (in blue) and metallic W was plotted in (green). The dashed lines are a guide to the eye.

Considering the roughness via Wenzel's equation, the modified contact angle, calculated surface potential and surface charge density were shown in Figure 4.4 in supplementary information. The modified contact angles plotted via cosine values exhibit quite similar trends for fuzzy and metallic tungsten, thus the major difference in Figure 4.3(a) can be attributed to roughness. It was known that the (θ) exhibits a maximum in close correspondence to the pH_{pzc} – the pH at which the net charge on the surface is equal to zero, where the surface energy would be a maximum, and in line with the expectations from the Lippmann variation. The relative contact angle variation between metallic and fuzzy W may be attributed to the differing surface charge characteristics. The specific free energy of the solid-liquid interface in the presence of surface charge was shown by Fokkink and Ralston[101]

$$\gamma_S L = \gamma_S L^0 + \Delta F_{dl}$$

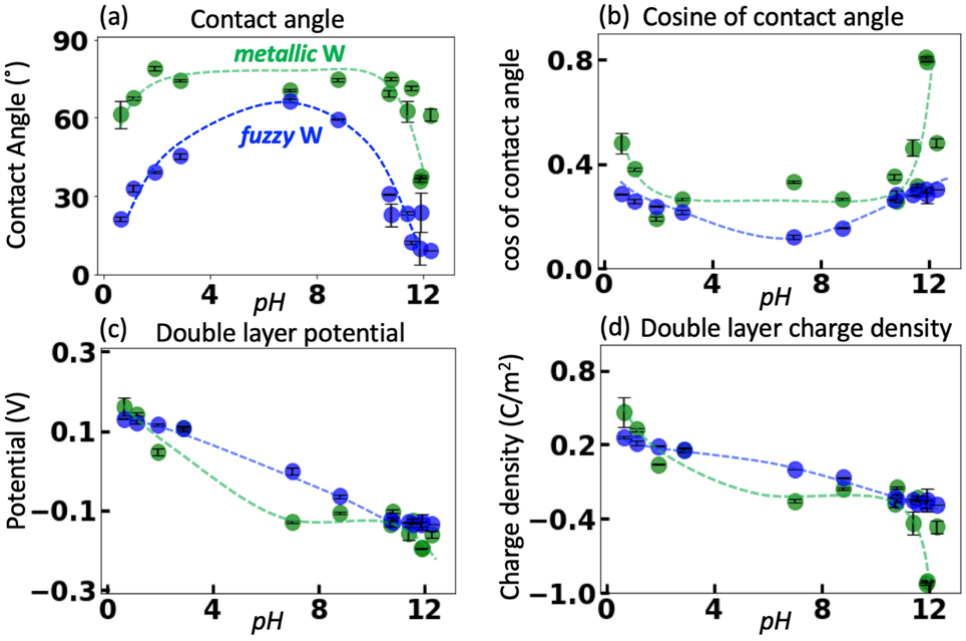

Figure 4.4: The variation of the contact angle (θ), cosine of contact angle, double layer potential (ϕ) and double layer charge density (σ_s), for (a) – (d): fuzzy W in blue and metallic W in green, as a function of pH. The dashed lines are a guide to the eye.

where ΔF_{dl} represents the free energy of formation of the ionizable surface relative to the pH_{pzc} for an ionizable surface with acidic or basic groups, where H^+ is the potential determining ion. The specific surface free energy ΔF_{dl} is

$$\Delta F_{dl} = \int_0^{\sigma_0} \Phi_0^D d\sigma - \int_0^{\sigma_0} \Phi_0^S d\sigma$$

The first integral on the right-hand side represents the electrical work for creating the electrical double layer, with σ_0 as surface charge density and Φ_0 as surface electrostatic potential, while the second is the chemical component of the free energy, which contains adsorption contributions to specific surface free energy. Since the chemical component is independent of the moles per unit area of adsorbed ions[102], this term becomes a constant.

$$\Delta F_{dl} = \int_0^{\sigma_0} \Phi_0^D d\sigma - \int_0^{\sigma_0} \Phi_0^S d\sigma = \int_0^{\Phi_0} \sigma d\Phi$$

Applied Gouy-Chapman model, the surface charge density (σ_0) may then be estimated:

$$\sigma_0 = \frac{4k_B T \varepsilon_0 \varepsilon_r}{\lambda_D e z_i} \left[\sinh\left(\frac{z_i e \Phi_0}{2k_B T}\right)\right]$$

k_B is the Boltzmann constant, T – the temperature, ε_0 - the permittivity of vacuum, ε_r - the relative permittivity of the solution (80), e – the unit of electronic charge, and z_i – the valence of the ion (=1). Inserting the previous eqn., the specific surface free energy ΔF_{dl} can be expressed as: the ion (=1). Inserting the previous eqn., the specific surface free energy

$$\Delta F_{dl} = \frac{4k_B^2 T^2 \varepsilon_0 \varepsilon_r}{\lambda_D e^2} [\cosh(\frac{z_i e \Phi_0}{2k_B T}) - 1]$$

Using the Young-Dupre equation, $\Delta F_{dl} = \gamma_{LV}(cos\theta - cos\theta_{max})$ Here, $\Delta cos\theta_W$ = r $\times \Delta cos\theta_m$ = r $\times (cos\theta_m - cos\theta_{m.max})$ and r is the roughness of the surface. θ_m the measured contact angle and $\theta_{m.max}$ maximum. Incorporating the θ along with the modulation of the surface potential in the was previously derived[103] to be:

$$\gamma_{LV} \Delta cos\theta_W = \frac{4k_B^2 T^2 \varepsilon_0 \varepsilon_r}{\lambda_D e^2} [\cosh(\frac{z_i e \Phi_0}{2k_B T}) - 1]$$

Consequently, the θ may be determined and are both plotted in Figure 4.3(b). Nominally, at or below a pH of 7, the dominant ions are H^+ and impart a positive charge to the double layer. However, a clear minimum θ is observed only in the fuzzy W around a pH of 7 and is not as pronounced for metallic W which has negative net charge accumulation below pH 7. The negative charging may be attributed to spontaneous dissociation occurs for intrinsic tungsten, as indicated in the Pourbaix diagram (Figure 4.5). As pH higher than 7, the OH^- group becomes the dominant and both fuzzy and metallic W have negative net charging. Their difference starts to come out above pH 11, the maximum value of negative net charging on metallic tungsten is 0.7 C/m^2 higher than that of fuzzy tungsten may be caused by dissociation. The effect of pH on solid-liquid interfacial tension lead to charge regulation at the solid-liquid interface to cause contact angle variation. The stronger negative charging of metallic tungsten indicate that it has a stronger affinity to potential determining ions OH^-. Meanwhile, fuzzy tungsten has a more robust performance under extreme pH condition. A significantly improved surface resistance to

water is then indicated for fuzzy W and indicates the promise of long-term stability for water splitting related materials[89].

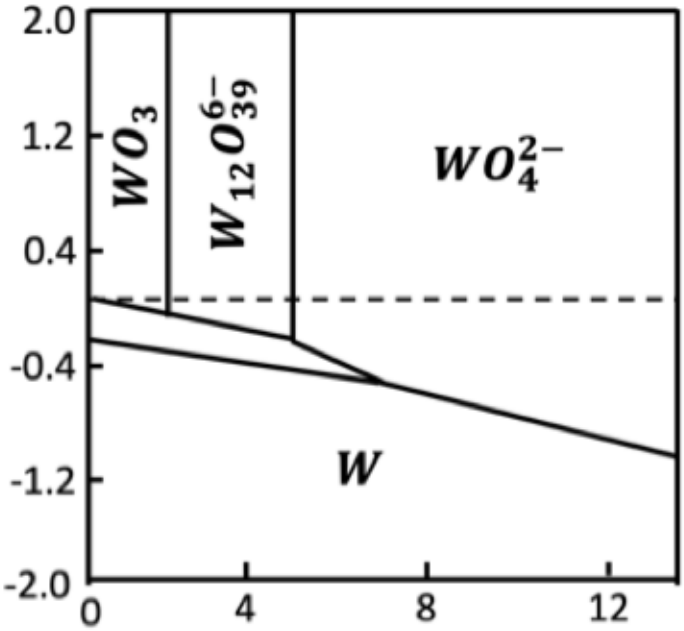

Figure 4.5: Pourbaix diagram

For solid-liquid interfaces, the electrical double layer as a function of potential determining ions has been studied through contact angle analysis. As an electrode, another characteristic aspect of the nature of the surface may be monitored through applied electrical field on tungsten: Figure 4.6. The slopes corresponding to the positive and negative branches of the charge (Q) – voltage (V) is related to an effective capacitance, with a larger value corresponding to closer approach of the ions, and the minimum refers to the potential of zero charge (PZC). At voltages either side of the PZC, the σ_s is net positive or negative. It was noted that the PZC for all the electrodes (metallic and fuzzy W as well as a reference Pt) was at a negative voltage with respect to the SCE, i.e., metallic W: - 0.333 V (-0.089 V: NHE), and fuzzy W: - 0.563 V (-0.319 V: NHE): see Figure 4.6. PZC is physically translated in terms of the work function. The values in brackets refer to the potentials with respect to the normal hydrogen electrode (NHE), which is about 4.44 V with respect to the vacuum. The implication is that, in solution, that the work functions of all

the metallic surfaces are ¿ 4.44 V, and hence negatively charged. It is also known that the work function is significantly modified in aqueous solutions[104], e.g., as a function of the extent of coverage and the configuration of the water molecules[105]. In the case of Pt, for instance, the obtained PZC value is close to the -0.35 V computed assuming significant structural changes in the solvation medium[105].

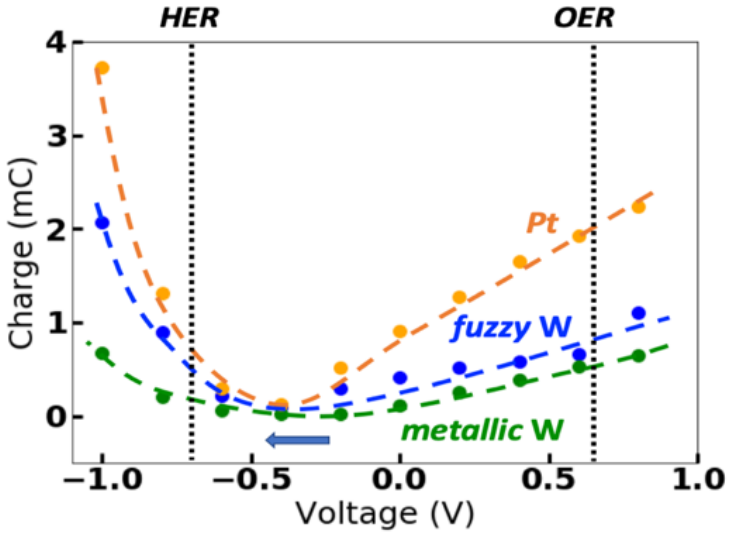

Figure 4.6: Indication of the potential of zero charge (PZC) for reference platinum (in orange), metallic tungsten (in green), and fuzzy tungsten (in blue). The black dotted lines represent the hydrogen evolution reaction (HER) and oxygen evolution reaction (OER) potential vs. SCE. The charge magnitude was obtained through chronocoulometry. The collected data points based on three parallel experiments; the error bar is below the resolution. The lines are a guide to the eye and the minima correspond to the PZC.

4.4 Charging characteristics via frequency dependency

The effective work function of the Pt at 4.78 eV (4.44 + 0.34) is significantly lowered from the vacuum value of 5.65 eV and is expected from water adsorption at the metal surface[104]. Generally, the work function originates from the contributions of the surface dipole and the electrochemical potential. Through our measurements, an effective value of the work function of 4.53 eV (4.44 + 0.09), was measured for metallic W, which is in accord with

previously reported values of 4.55 eV[106]. An increase in the effective work function to 4.76 eV was observed in fuzzy W, which should be compared to a previously reported value of 4.94 eV[60]. A plausible increase in the work function in fuzzy W was posited to be due to the strong repulsive potential from incorporated He[107]. Moreover, the nanostructured surfaces in fuzzy W yield a curvature and a consequent rearrangement of the water dipoles with respect to a flat surface. While concave surfaces/ concave nanostructures (i.e., due to the interstices in the surface) are thought to be responsible for an effective decrease in the work function, the protrusions (i.e., yielding a convex curvature) would increase the work function as observed. The increased value close to that of Pt, due to the combination of structured surfaces, size-related effects, as well as possible adsorbates, is remarkable. It has been previously indicated[108] that the surface structure as well as the shape may play a role in determining the PZC indicating the influence of the local interactions.

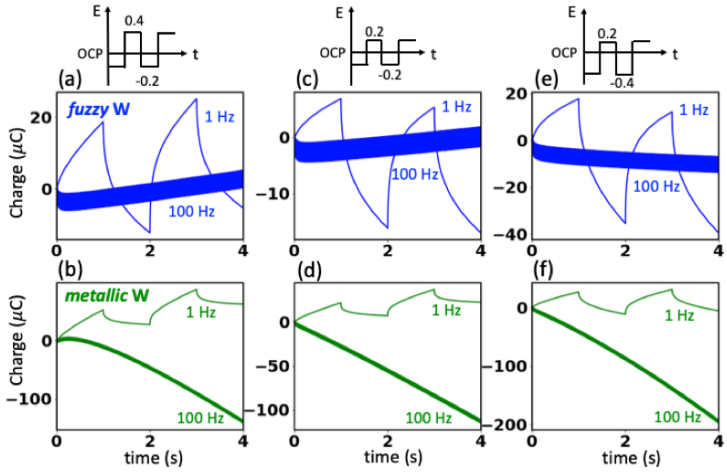

Figure 4.7: Charging characteristics of fuzzy W (a), (c) and (e) and metallic W (b), (d) and (f) based electrodes probed through chronocoulometry (CC) at a pH of 7. Here, the voltage was modulated between V_1 and V_2, where V_1 (V_2) is a voltage positive (/negative) to the PZC potential. The voltage-time profiles are inset. For illustration, the response at low frequency (1 Hz) and high frequency (100 Hz) are indicated.

We compare the charging characteristics of fuzzy W based metal electrodes with metallic W electrodes in static state in previous sessions. For the purpose of dynamic charging study, a voltage (V) vs. time (t) schedule around the respective PZC was deployed. Here, the voltage

was modulated between V_1 and V_2, where V_1 (V_2) is a voltage positive (/negative) to the PZC potential. We indicate through Figure 4.7, the range of frequency at which the voltages were cyclically applied, i.e., 1 Hz and 100 Hz, where it was generally observed that less charge is stored at higher frequencies as expected. Moreover, the charging behavior was seen to vary with the particular surface, i.e., fuzzy vs. metallic W.

For instance, considering the 1 Hz data, there is always a progressive charging of the metal W surface irrespective of the polarities of the V_1 and V_2: Figure 4.7 (d). However, a different behavior was observed for fuzzy W surfaces where if $|V_1| < |V_2|$, a progressive discharge was indicated: Figure 4.7(a). An initial applied voltage positive (/negative) of the PZC would induce negative (/positive) charges on the metal surface. However, such interchange involves the ingress/egress of the relevant ions which is kinetically limited and accounts for the frequency dependence. There are two major groups of ions in the electrolyte: H+ and OH- have similar mobility: 3.6×10^{-7} m^2/Vs and 2.0×10^{-7} m^2/Vs, K^+ and Cl^- have almost unique mobility of 7.7×10^{-8} m^2/Vs that makes it a widely used electrolyte. For both metal/fuzzy W, when $|V_1| > |V_2|$: Figure 4.7(a) and (d) the positive voltage (e.g., V_1 = 0.4 V) attracts Cl^- and OH^- ions while the negative voltage (e.g., V_2 = - 0.2 V) attracts K^+ and H^+ ions. A progressive positive (/negative) charging indicates a net accumulation of K^+ and H^+ (/Cl^- and OH^-) at the surface. Such positive charging was always seen for metallic W irrespective of the relative magnitudes of V_1 and V_2, implying an overall accumulation of the positive ions: Figure 4.7 (b), (d) and (f). One possible reason is the smaller size of the K^+ (0.138 nm) compared to the Cl^- (0.181 nm), which diffuses easily and is attracted to the net negative charge of metal surfaces. However, at higher voltage scan rates (say, 100 Hz): Figure 4.7 (b), (d), and (f), the dissociation of tungsten is apparent and related to a net negative charge accumulation[109]. On tungsten surface, the accumulation of dissociation product WO_4^{2-} prevents further dissociation. However, for high frequency, fast flipping the sign of charge at the interface leads to a fast replacement of ions for metallic tungsten. As a result, WO_4^{2-} ions can be pushed away and fresh tungsten surface

exposes, as well as promoting the dissociation.

A different type of behavior is seen in the fuzzy W, where at low voltage scan rates there is a net positive charging only when $|V_1| > |V_2|$: Figure 4.7 (a). The nanostructured characteristic of the surface, coupled with the attendant tortuosity, makes free ion movement difficult with the consequence that a net negative charging is seen generally, i.e., for $|V_1| < |V_2|$: Figure 4.7 (c) and (e). At higher frequencies, there is generally a net accumulation of positive charge as well as a greater modulation of the charge – as given by the amplitude of the variations, compared to metallic W. Such an aspect is hypothesized as due to internal surface charging, considered from a thin layer electrochemistry (TLE) aspect[99, 110] in Figure 4.7 (a), (c) and (e). The negative charge accumulation in each period is due to the sluggishness of the Cl^- ions.

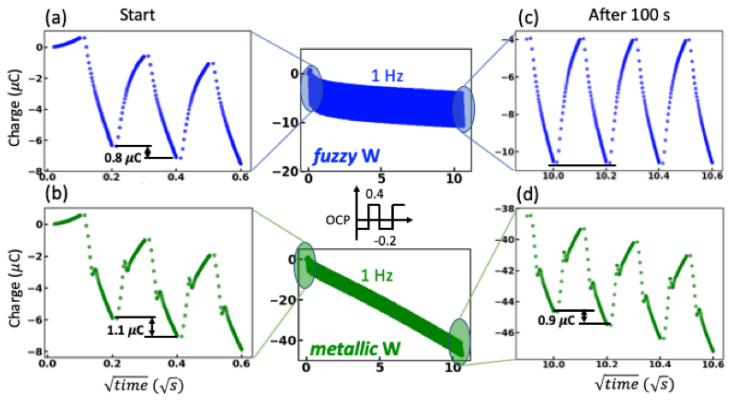

Figure 4.8: Charging characteristics of metallic and fuzzy W based electrodes probed through chronocoulometry (CC) at a pH of 7 for the 100 Hz voltage scan rate. (a) and (b) relate to the charge-discharge characteristics at the beginning of the experiments for fuzzy (in blue) and metallic (in green) tungsten, while (c) and (d) indicate the charge-discharge characteristics after 100 seconds.

In more detail, as shown in Figure 4.8 (a) – (b), initially, both fuzzy and metallic tungsten have negative net charge accumulation, 0.8 and 1.1 μC, respectively, in a given charge-discharge cycle. However, subsequently after 100 seconds of continued cycling, the charge accumulation is considerably reduced for fuzzy W: Figure 4.8 (c), while negative charge of similar magnitude persists for metallic tungsten: Figure 4.8 (d). Consequently, the net charge accumulation in the metallic W may be ascribed to the formation of WO_4^{2-}, as previously discussed. In contrast,

limited dissociation occurs in the fuzzy tungsten case. The additional stability introduced by fuzzy structure is consistent with the conclusion of contact angle measurement. In addition, although the mobility of K^+ and Cl^- is almost identical, due to the relative larger mass of Cl^-, its frequency response would be slower than K^+. Thus, a plausible explanation for the net negative charge accumulation is that chloride ions are trapped into the fuzzy nano-structured surface and further protect W from oxidation by repulsing OH^- away.

4.5 Conclusion

In summary, our work indicates that surface engineering through helium plasma bombardment is a viable technique for modulating the charging characteristics of metal surfaces. It was shown here that it would be possible to significantly alter the charge states, e.g., through modulating the PZC, as well as the kinetics of charge transfer, e.g., as manifested in the variation with respect to the voltage cycling rate, through surface modification. It was also shown that contact angle modulations could be transduced into the relative changes of the surface potential and charge density. While the rate constants could provide one measure for the observations, more detailed interpretation requires detailed knowledge of the local chemical equilibria as well as physical attributes related to local curvature and roughness. The present work, supplemented by such investigations would be of much utility in exploring further the electrical interface[111] at the electrodes with implications to enhancing the capacitance as well as the charge capacity and energy storage.

4.6 Experiments and methods

Synthesis of fuzzy tungsten. He induced fuzzy tungsten samples were prepared from polycrystalline tungsten discs (2 cm in diameter and 1.5 mm in thickness). After polishing and

ultrasonic cleaning, the discs were exposed to low energy and high flux He plasma (5×10^{18} $cm^{-2}s^{-1}$, with an energy of 60 eV), from an arc discharge[57, 58], for 30 minutes and a temperature of 1600 K, to generate the fuzzy nanostructure. The He plasma was generated in the Pisces-A chamber that produces a He ion flux from an arc discharge[57, 58].

Contact angle measurement. A Ramé-Hart Model 190 Goniometer was employed for contact angle measurements. A charge-coupled device (CCD) camera was used to image and quantify the contact angle, and the reported averaged over multiple measurements. The wetting characteristics of tungsten and platinum were measured in 0.1 M KCl electrolyte, under various pH values. The pH of the electrolyte solution was adjusted to specified values by addition of small amounts of acid (hydrochloric acid) or base (sodium hydroxide).

Electrochemical characterization and analysis. All the electrochemical experiments were performed via Gamry (PCI4) potentiostat. Chronocoulometry (CC) was applied to measure the charge vs. time response to an applied potential step waveform. In our experiments, CC measures the charge (time integrated measured current), utilized currents measured with varying amplitude of applied square-wave potentials (+/- 0.4 V) around the voltage corresponding to the point of zero charge. The charging properties were investigated under 1 Hz and 100 Hz in multi-stepped CC. The voltammetry of tungsten and platinum were performed in 0.1 M KCl salt electrolyte. A three-electrode setup with the working electrode (Pt, metallic W, or fuzzy W), counter electrode (Pt foil $1cm^2$) and SCE (standard calomel electrode) reference was used. 10mM $K_4Fe(CN)_6$ to serve as the electroactive redox component.

4.7 Acknowledgement

This chapter has been prepared as ”Static and dynamic charging characteristics of nanoscale fuzzy tungsten surfaces.” by Chen, P., J. Sigurdson, M. Baldwin, and P. R. Bandaru is under revision. This work was supported by a grant (CBET 1606192) from the National

Science Foundation (NSF). P.C. and P.R.B. contributed to the conceptualization, experimental design, and the development of the project. P.C. carried out the electrochemical measurements, while P.C. and M.B. synthesized the fuzzy tungsten samples. P.C. and P.R.B. wrote the paper.

Chapter 5

Iron redox pathway revealed in ferritin via electron transfer analysis

Ferritin protein is involved in biological tissues in the storage and management of iron - an essential micro-nutrient in the majority of living systems. While there are extensive studies on iron-loaded ferritin, its functionality in iron delivery is not completely clear. Here, for the first time, differential pulse voltammetry (DPV) has been successfully adapted to address the challenge of resolving a cascade of fast and co-occurring redox steps in enzymatic systems such as ferritin. Using DPV, comparative analysis of ferritins from two evolutionary-distant organisms has allowed us to propose a stepwise resolution for the complex mix of concurrent redox steps that is inherent to ferritins and to fine-tune the structure-function relationship of each redox step. Indeed, the cyclic conversion between Fe^{3+} and Fe^{2+} as well as the different oxidative steps of the various ferroxidase centers already known in ferritins were successfully discriminated, bringing new evidence that both the 3-fold and 4-fold channels can be functional in ferritin.

5.1 Introduction

Ferritin is an ubiquitous protein[29, 30] involved in the storage and management of iron - an essential micro-nutrient for almost all living systems. The protein occurs in abundance in the cytosol and mitochondria, where it helps maintaining the performance of critical biochemical reactions[112–115] and balance oxidative stress processes[116]. Ferritin is therefore mainly internal in most systems, but can sometimes be a secreted enzyme[116], and can thus be used to manage balance of iron both intra- and extracellularly, which can protect from deleterious excess of iron uptake, but also from viral and bacterial infections. Ferritin is known to take up iron (as Fe^{2+}) and store it in stable unreactive Fe^{3+}-oxide/hydroxide form (primarily ferrihydrite). It is believed to deliver Fe back in a functional Fe2+ form, where and when needed for biological processes[28]. In spite of many biochemical studies on performance of loaded ferritin, some parts of the molecular mechanisms of iron uptake, e.g., associated with oxidation steps, and most of the iron release and delivery, e.g., associated with reduction steps), remain largely unclear and speculative[28, 117–119].

5.2 Ferritin structure in HuHF and ChF

Structurally, ferritin is a biomacropolymeric enzyme constituted of 24 subunits (Figures 5.1 (a) and (b)) forming a hollow structure – often referred to as a cage that can be loaded12 with Fe. The cage has an octahedral (432) symmetry where the 4-fold and 3-fold axes of symmetry are the place where 4 and 3 subunits meet together to respectively delineate six four-fold channels and eight three-fold channels. These channels have a small diameter (ranging from 0.2 nm to 0.5 nm) that varies along the 3 - 4 nm length of the channels. To date both the 3-fold and 4-fold channels have been considered for the Fe^{2+} ion entry into the core of the cage, but proof of natural activity[28, 31, 119] has been delivered only for the 3-fold channels. There are three types of ferritin subunits: Light (L), a Middle (M) and a Heavy (H) subunit, in increasing order

of molecular weight. Ferritin cages are usually constituted of a mix of Light and Heavy chain ferritins. Other ferritins only consist of a single type similar to the heavy chain. In the center of all except the L-type ferritin subunit, a ferroxidase site (capable of oxidation and possibly reduction) was identified through multiple mutation studies[28], containing two prominent Fe binding and oxidation sites, named site A and B (after their affinity for Fe): Figures 5.1 (c) and (d). A third metal binding site is observed in several crystal structures, referred to as the C site. This C site is not usually considered associated with ferroxidase activity but would play a role as a gateway in the passage of the iron as a transient form to the ferrihydrite stage for final storage[28].

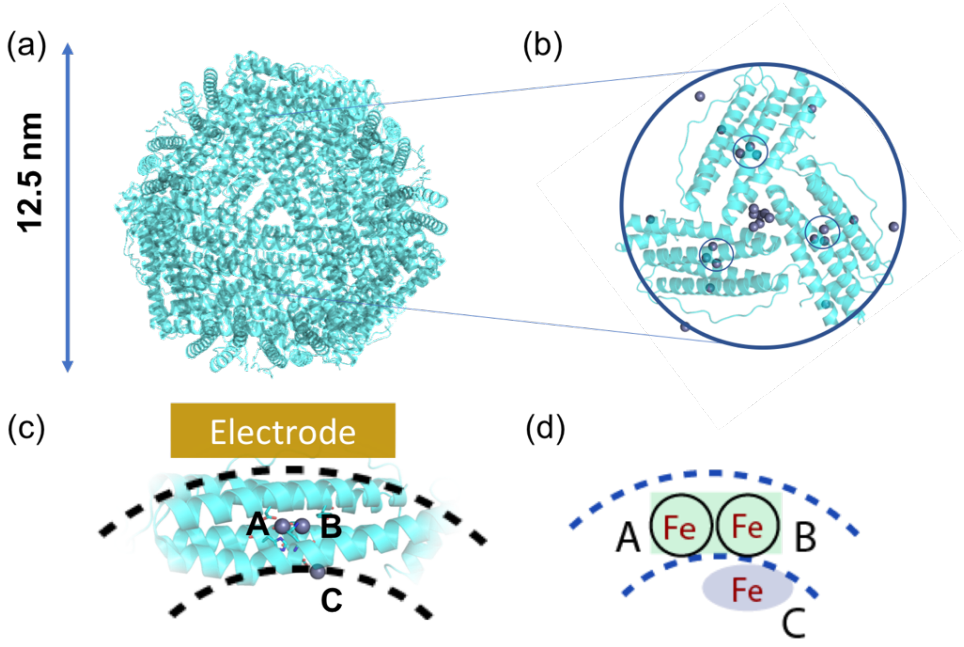

Figure 5.1: Ferritin structure and related iron binding sites, (a) The crystal structure of a ferritin cage, with the 24-subunit ensemble spanning 12.5 nm. Each subunit carries a ferroxidase center buried inside a four-helix bundle. (b) Three ferritin sub-units indicating the four-helix bundles delimiting a 3-fold channel and displaying metal ions (purple) at the location of the ion channel and the ferroxidase site (indicated with circles). (c) The Fe^{2+}/Fe^{3+} binding sites: A and B constitute the ferroxidase center, and site C is a ferrihydrite nucleation/gateway site. The dashed lines represent the cross section of the 24-meric cage (shell). (d) A schematic representation of the A, B, and C sites, within a ferritin shell. All crystal structure representations are made in PyMol14 based on 2CIH.pdb[120]

The amino acids interacting with the metal ions in these three key sites delineate the ferroxidase site in which the oxidation of Fe^{2+} to Fe^{3+} takes place when taking up iron, and

potentially also the reductive step of Fe^{3+} to Fe^{2+} when releasing, although some ambiguity exists on the exact mechanisms related to the redox dynamics[33, 34], especially when considered under the influence of external reducing agents[18]. Aside from bacterioferritins, most studies on Fe ion dynamics have been done on horse (equine) ferritin because of large availability, as well as on human ferritins because of the incentive to understand the critical role of ferritin in human diseases[121]. Consequently, crystal structures of less than 20 different eukaryotic ferritins are available, and both structures and kinetics studies of homopolymers across species have always reported similar properties, thus rendering the establishment of natural structure-function relationship relative to performance rather challenging, but also irrelevant. After all, the ferritin system machinery, as found in most eukaryotes appeared to have evolved to the ultimate perfection and most mutations studied are deleterious. Recently, a ferritin (Chaetopterus ferritin, ChF) was found associated with the production of visible light (bioluminescence) in the secreted mucus[2, 3] of the marine tube worm Chaetopterus sp[2]. Interestingly, this was the first natural eukaryotic ferritin found to significantly outperform human heavy chain ferritin (HuHF) - a conventionally accepted representative of a vertebrate ferritin, for ferroxidation velocity, being up to eight times faster[3]. This discovery however provided the first natural eukaryotic "out of the ordinary" ferritin that could be used as a tool to understand the mechanistic pathways in ferritins, which could be critical for some medical as well as biotechnological applications[119, 122–124]. From a biochemical point of view, the Fe^{2+} transportation mechanisms into and out of the ferritin core, and the related electron movement associated with reduction steps, are not yet entirely understood[31, 35]. A better understanding of charge transfer processes is clearly needed to pave the way for a more complete assessment of ferritin functionality and establish structure-function relationships in relation to electron transfer at the molecular level. Mossbauer spectroscopy[117] as well as EPR-spectroscopy[125] have been previously applied to study ferritin-related mechanisms. While the iron oxidation states inside the ferroxidase center were revealed, the path of electron transfer remained unclear from these analyses. Electrochemical

methods such as cyclic voltammetry have also been applied to study molecular chemistry of ferritins, yet due to the difficulty of observing charge transfer between electrode and ferritins, such experiments had to be performed using redox mediators, thus making the identification of electron paths challenging[126].

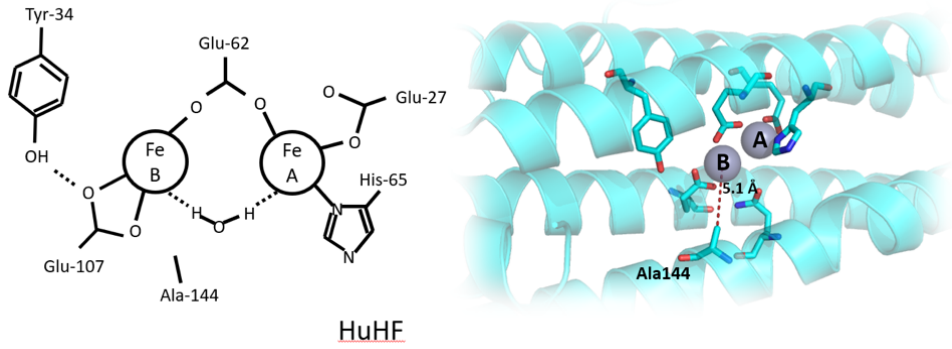

Figure 5.2: The coordination environment of the A and B sites in HuHF

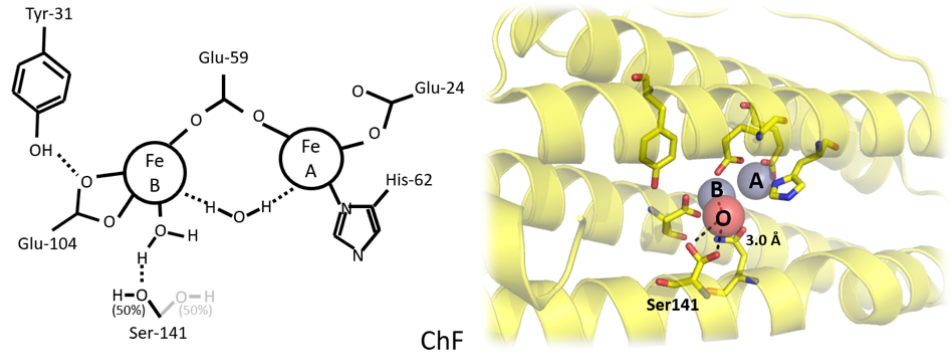

Figure 5.3: The coordination environment of the A and B sites in ChF. 5WPN shows 50% dual conformation for Ser-141 (indicated in grey).

The specificity of A and B sites, relevant to HuHF and ChF, in the electrochemical analyses, were inferred from the relative position of the anodic peak/s, where A (/B) is more electro-positive (-/negative) due to the N-(-/O) coordination.

HuHF cage viewed from the inside of the sphere up the four-fold axis in Figure 5.4 (a), with four subunits in cyan and the surface of the residues in the path between the four-fold

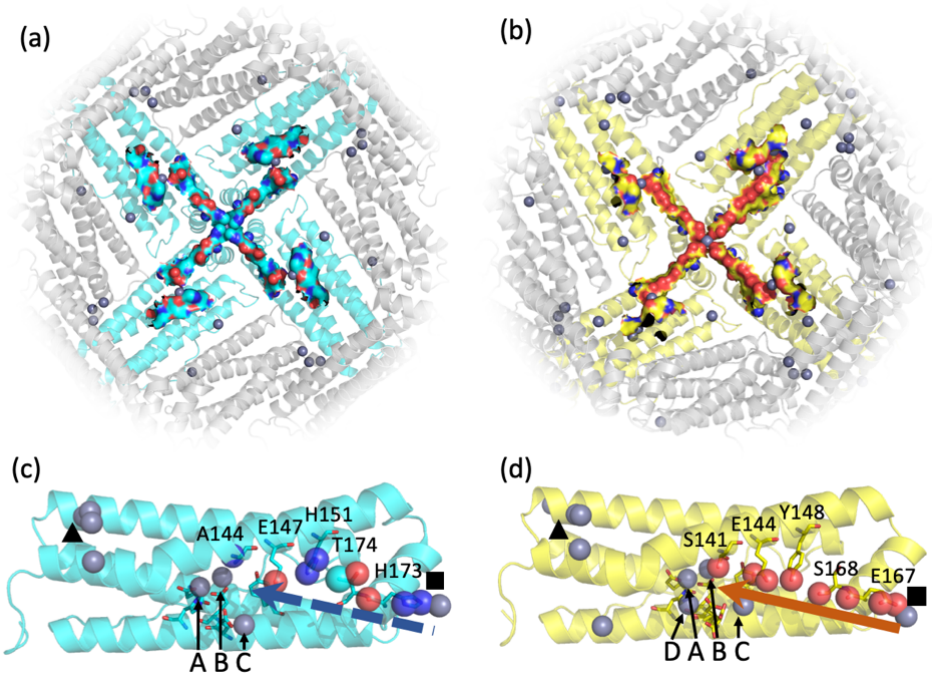

Figure 5.4: (a) four-fold axis in HuHF, (b) four-fold axis in ChF

channel and the respective ferroxidase sites. The residues are displayed through "sticks" and their available atoms at the inside surface of the ferritin shell are displayed in spheres, i.e., Red: oxygen, dark blue: nitrogen, cyan: carbons in HuHF, grey spheres: metal ions. In Figure 5.4 (b) ChF cage viewed down the four-fold axis, with carbons in yellow. A clear bright red path is extant between the four-fold channel and the ferroxidase sites. Figure 5.4 (c) and (d) are monomers of HuHF and ChF, respectively. The red spheres in (d) show the hydroxide groups available for binding Fe (grey spheres) on its way to the ferroxidase center. In Figure 5.4 (c) corresponding atoms are represented in spheres (color coding – see above), only a minority of which are OH groups. The arrows indicate the direction of putative ion flow towards the ferroxidase center. A black square and triangle are added to indicate where the four- and three-fold symmetry axes or channels are respectively located, within the subunit. All figures were generated in PyMol1. 2CIH was used for HuHF and 5WPN for ChF.

5.3 Differential pulse voltammetry (DPV) study in biological charge transfer

To probe the redox mechanism of the high-performing ChF ferritin, we decided to use voltammetry methods. Since the kinetic processes in ferritin are quite rapid (within 50 ms)[127], conventional voltammetry methods such as cyclic voltammetry with a fast scan rate ($>$ 50 V/s) were deemed insufficient. The approach of differential pulse voltammetry (DPV) was applied instead to measure and integrate coupled processes related to ferritin species related transport to the electrode[18]. While DPV is developed for the measurement of small concentrations, we here take advantage of the stepwise pulsed voltage increases to enhance the sensitivity and specificity of the response and help address the issues related to deformation and adsorption of ferritin protein to electrodes surface. Considering the relative structural complexity of the ferritin protein and that the active ferroxidase sites are buried relatively deep within the ferritin, one can assume ferritin related voltammetry[5] to be integrating multiple scales and types of events, e.g., related to charged species transport to the electrode, relevant enzyme kinetics, as well as interfacial electron exchange[20] each of which rate limiting in its own time and spatial scale[27]. In this work, we combine comparative analysis of HuHF and ChF crystal structures with electrochemical analysis aiming to (1) better understand the flow of electrons in both ferritins in association with the DPV redox kinetics of iron, as well as to (2) determine which electrochemical step and/or pathway of the ferritins are different enough to sustain the measured difference in ferroxidase activity between HuHF and ChF. We decided to use the homomultimeric form of HuHF rather than work with a mix containing light chain ferritin, in order to make sure measurements were made on a simplified system with no protein-protein interactions (between heavy and light chains) that could interfere with our data interpretation.

Voltammetry of the ferritin complex measures and integrates coupled processes related to charged species transport to the electrode, relevant enzyme kinetics, as well as interfacial

electron exchange – each of which may be rate limiting[20]. The redox kinetics of ferritin were previously recorded as subject to a variety of factors, including pH, surrounding buffer content, and long-range electron transfer through the protein matrix[18]. Our approach primarily consists of the parameterization of redox behavior in terms of the relative number of the Fe ion species (Fe^{2+} or Fe^{3+}) with respect to the protein. In the work reported here, recombinant ferritin with around 10 Fe ions per cage was used to probe for charge transfer between ferroxidase center and electrode. The core Fe related processes were not considered in our investigations. As indicated in the Methods section, voltammetry measurements from native ferritin (10 Fe/cage average load) and slightly loaded ferritin (31-32 Fe/cage average load) showed identical peaks.

Differential pulse voltammetry (DPV), was selected to probe the electrochemical characteristics of the ferritins with increased species-specific sensitivity[26]. Description and interpretation of typical recordings of the voltammograms are detailed in Figure 5.5.

Control experiments were performed to identify potential contributions from apoferritin (without Fe inside the core), free Fe^{2+} ions as well as ions bound to hydroxides, from those related to the ferritin bound Fe^{2+}/Fe^{3+} ions. Figure 5.5 (b) indicates the redox processes obtained, in the cathodic and anodic scans, by adding $FeCl_2$ yielding $Fe(OH)_3/Fe(OH)_2$ pair in aqueous background solutions. The labeled redox peaks observed in the low voltage range (centered at -0.54 V) are related to the redox pair Fe (OH)3/Fe $(OH)_2$, and the redox peaks centered at 0.2 V are related to the $Fe^{2+}/Fe(OH)_3$. Free Fe^{2+} ions are unstable at pH = 7, where they undergo auto-oxidation and precipitate into ferric hydroxide. A ChF ferritin DPV signal - outer lines in Figure 5.5(c) was clearly measured and distinct from the background baseline, which is the phosphate buffer by itself - inner lines in Figure 5.5(c). The ChF ferritin DPV signal appeared with more details (Figure 5.5d) when the background (buffer) was subtracted from the signal curves. The redox potential measured is quite close to that of Fe $(OH)_3$/Fe $(OH)_2$ and such a redox pair only exists in the ferritin with iron ions (See Figure 5.6 for comparison with apoferritin). Supporting our findings, another mechanistic study[117] yielded similar redox potentials, confirming that the

signal detected in our ferritin samples is indeed from iron going through chemical transformation inside the ferritins. Consequently, our results report with high fidelity Fe ion redox dynamics internal only to the ferritin.

The DPV of HuHF, ChF and commercialized available Equine spleen Apoferritin (ApF) are indicated in Figure 5.6, below. The cathodic and anodic peak amplitudes of HuHF and ChF are much higher than Apoferritin, corresponding to the greater abundance of iron, in the former. The correspondence to specific A and B sites, relevant to HuHF and ChF, respectively are inferred from the relative position of the anodic peak/s in Figure 5.5. The negligible ApF related signal indicates the absence of iron. It may be concluded then that the related detected signals for ChF and HuHF (in Figures 2-4 of the main text) are ferritin specific.

5.4 Redox kinetics in HuHF probed through DPV

We first discuss the DPV involving dissolved HuHF (Figure 5.7), and then subsequently compare with the kinetically faster ChF. When following the voltammogram of HuHF (Figure 5.7 (b)), which started with a cathodic scan, followed by an anodic scan, the reduction and oxidation signals related to the iron inside the ferritin appeared at a pronounced current change, at the relevant applied voltage. The cathodic peak was deconvoluted into two subsidiary peaks designated A and B (Figure 5.7 b); peak B being at slightly more negative voltage than peak A. The basis for the deconvolution was the asymmetrical shape of the cathodic peak in both the HuHF and ChF DPV. We used appropriate peak fitting procedures, e.g., using second order derivatives, and OriginLab multi-peak fitting tools to yield two sharp peaks related to the A and B peaks in the cathodic scan, while such peak delineation was absent in the anodic scan.

In Figure 5.7, Orange arrows indicate the direction of electron flow, while green arrows indicate iron ion flow. The cathodic processes (reduction, top) at the two Fe^{3+} (in red) ions associated with the (II) A and (III) B sites yield two peaks corresponding to the creation of two

Fe^{2+} ions (in blue) at the end of the cathodic scan. (IV) One of the formed Fe^{2+} is transported away from the ferritin and is (V) replaced by the Fe^{3+} from the C site or from the core (no specific proof of this was found in DPV). In the voltage-driven anodic process (bottom), (VI) the residual Fe^{2+} is oxidized to Fe^{3+} at site A only (when little Fe^{2+} is available) and constitutes the one peak observed in the anodic scan. (VII) The rearrangement of Fe^{3+} supplies the iron to the C site or to the core. Depending on the abundance of external free Fe^{2+} (limiting vs not limiting), the ferroxidase site can either remain vacant with limited free Fe^{2+} or take up iron and oxidize it when free Fe^{2+} is available abundantly, as shown in (VIII) and (IX). Three possible pathways have been indicated for the oxidation. The top path (in dashed lines) represents the fast, natural oxidation taking place inside the ferritin in the time frame between the cathodic and anodic scans. The two others are the voltage-driven reactions, associated with the voltammogram.

We propose peak A and peak B to be associated with Fe bound in sites A and B of the ferroxidase center[28, 32], respectively; cf. Figures 5.1 (c) and (d), and Figure 5.7 (a). While the two iron atoms in the ferroxidase center have similar chemical environment, the B site is coordinated through acidic groups (Glutamates) only, in contrast with the A site that is coordinated through acidic as well as an alkali groups (Histidine 65)[3, 31, 35]. This results in making the site B site slightly more electronegative than site A and is invoked to explain the different peak positions observed in the voltammograms: Figure 5.7 (b) and Fig. 5.8 (b). After reduction in the initial cathodic scan, Fe^{2+} is re-oxidized by the ferritin and potentially even auto-oxidized in the buffer, leaving only a small amount for the oxidation during the anodic scan, resulting in a smaller amplitude of the anodic peak. The anodic peak cannot be deconvoluted at this stage and was labeled “peak A”, since the only logical and coherent option in relation to the peak A observed in the preceding cathodic scan, and in line with expectations of closely spaced redox pairs[24].

5.5 Redox kinetics in ChF probed through DPV

The cathodic processes (top) at the two Fe^{3+} ions are associated successively with the (II) A and (III) B sites and yield two peaks corresponding to the Fe^{2+} and Fe^{3+} rearrangement at the end of the cathodic scan (IV), involving the D site. One of the formed Fe^{2+} ions is then transported away from the ferritin and (V) site A is occupied by Fe^{3+} from inside the ferritin. In the anodic oxidation process, (VI) the residual Fe^{2+} is oxidized to the Fe^{3+} in site B and constitutes the one peak observed in the anodic scans. (VII) The oxidized iron supplies the Fe^{3+} to the inner iron site. (VIII) and (IX) are follow-up steps when free Fe^{2+} is available.

Integral to the alternative pathway is another metal binding site - arbitrarily labeled “D” in Figure 5.8 a, proximate to the A site, and found in the ChF crystal structure[3]. Comparison with over 30 other available crystal structures of eukaryotic (heavy chain) ferritins shows that this is a unique configuration. As is often done in enzyme crystallography, Zn^{2+} was used as an inert substrate alternative with comparable size and charge as Fe^{2+} in the generation of the relevant 5WPN crystal structure[35, 120]. While this has proven to be a conventional approach for optimization of structural analyses, interpretation relative to the electrochemical function of structural features can be more challenging. For example, despite similar structural positioning of the A-B sites in the ferritins, the voltammogram for ChF (Figure 5.8 b) shows oxidation in the B site first, which can only could be rationalized by a pathway inside the enzyme involving the entry of Fe^{2+} ions into the ferroxidase site through the B site first, instead of the A site and oxidizing the Fe^{2+} ions in the B site such as for HuHF: Figure 5.8 (b). Ideally, in order for this mechanism to work while keeping the enzyme configuration in mind, the Fe ions have to enter and exit the ferroxidase center on the opposite side in comparison to HuHF: Figure 5.7 (c). Interestingly, it has been previously postulated[28] that site B may be accessible through the four-fold channel which has been proven a possibility through mutation studies[128, 129]. The activation of the four-fold channel in bullfrog ferritin enhanced the ferroxidase activity five-fold. A comparable enhanced

performance has been previously observed naturally in the wild type ChF[130]. Indeed, a detailed comparison of the crystal structure of HuHF reveals such a Glutamate and hydroxide rich path between the four-fold channel and the ferroxidase center, only in the faster ChF. As for metal ions exiting the ferroxidase site on the opposite side, the D site in the ChF crystal structure could be assigned the gateway site in this new pathway. Clearly this difference in electro-chemical mechanisms across sites between ChF and HuHF could only be detected using DPV and not structural analyses only. While previous work in our group has shown that ChF takes up iron considerably faster than HuHF, the present study shows that the related mechanism might be more drastically different than initially anticipated. The faster kinetics are not just explained by a few residues in the commonly accepted pathway but by a complete shift in the pathway to a faster entry for Fe^{2+} ions. Our study points out that the oxidation takes place in different sites (A vs. B) in the ferroxidase site in the ferritins, which can only be explained by entry of the Fe^{2+} ions from the opposite side (towards B site, instead of A), which is feasible through invoking the four-fold channel in ChF. After oxidation, the Fe^{3+} ions would exit the active site from the A site through the newly assigned D site and find their way to the core. Through voltammetric analyses, we were able to provide proof of the reducing capabilities of both sites in the ferroxidase center in both ferritins, reveal their differences, and shed light on the question as to where in the ferroxidase center the oxidation takes place and/or in which order.

5.6 Dynamics in iron active sites during iron loading

As it was previously estimated[27, 131], that the diffusion time of iron to the ferroxidase site is of the order of ms, the Fe^{2+} uptake into the ferritin is not manifest in such scans. In the cathodic scans, we discern the possible appearance of a subsidiary peak, the effect of which diminishes with time, and which may be related to additional iron site. There seemed to be a reversion to the pristine/unloaded HuHF form, coinciding with a disappearance of 0.26 V, after

about 48 hours. Generally, a peak component change observed in the cathodic peaks, from the presence of $FeCl_2$, in comparison to what was observed in Figure 5.7 (c). As a reveal of the ratio of peak A to B, highest after iron loading, then decrease, more charges transfer to the iron inside site B. This site could be quite active during iron loading. Meanwhile, the anodic peak from ferritin in absent during iron loading. The tendency for the saturation of Fe^{3+} in active sites during iron loading may likely be the underlying reason. Alternately, in the ChF, remarkable changes in the anodic and cathodic processes were indicated due to the $FeCl_2$ addition: Figure 5.9.

Distinct from HuHF, and evident from Figure 5.9 (a) and (b), the original anodic and cathodic peaks relevant to unloaded ChF are always present even in the presence of $FeCl_2$ addition. For the oxidation process, the 0.26 V peak was again seen, with peak magnitude changing with time in a similar manner to that observed in HuHF, albeit with the persistence of the oxidation peak from the pristine/unloaded ChF form. In the reduction scan, there arises a peak at a smaller voltage, - 0.35 V that is in Figure 5.9 (a) and (b). This peak gradually diminishes and merges with peak B indicating the physical basis of this peak could be attributed to the intermediate iron site during iron loading. At t = 2 and 48 hours, respectively, the ip_A/ip_C ratios, considered with respect to the original peaks, are 0.5, while the $W^A_{1/2}/W^C_{1/2}$ ratios are 1.20, respectively. The approach to unity, comparing to unloaded case in the current peak and the width ratios, and hence to increasing reversibility during iron loading, at t = 2 hours is of note. Unlike HuHF, the ferroxidase site is not saturated during iron loading in ChF. Despite of the appearance of the new peak in the cathodic scan, there is only one anodic peak comes about.

The above aspects are clearly indicative of distinct iron upload/download pathways in the ChF compared to the HuHF. A schematic diagram is shown in Figure 5.9 (d) and Figure 5.10 (d). Under the condition of abundant free Fe^{2+}, the Fe uptake process is different for ChF as a new Fe^{3+} state exists here, contributing to the acceleration of iron loading. As in the HuHF case, there is a conformational change inside ferroxidase center as shown in peak ration in Figure

5.10 (a) and (b). In addition, the ferroxidase center is saturated with Fe^{3+} in HuHF, while the charge transfer still behaves reversible in ChF. This pheromone could be further related to the iron deliver efficiency towards the mineral core. A saturated active site may be corresponded to a sluggish Fe^{3+} delivery. The additional cathodic peak in ChF can be attributed to the existence of other ferroxidase centers. It seems to be apparent from our observations that distinct redox mechanisms are observed in ChF compared to HuHF, with respect to the (a) greater degree of electrochemical reversibility of the Fe^{2+}/Fe^{3+} kinetics in ChF, (b) the formation of intermediate states of Fe^{3+} compound in iron loading processes of ChF. It may be the case, that in the ChF, the Fe^{3+} formation is more favored, e.g., typical to the storage of Fe in the ferritin core[131], as manifested in the persistence of the oxidation peak even after the addition of the $FeCl_2$.

5.7 Conclusion

This chapter yields considerable insight related to the molecular mechanisms of ferroxidase activity in ferritins. The benefit of integrating analyses for tailored biochemical performances across different animal species was demonstrated, where ferritin operates under different environmental constraints, through DPV - which for the first time was used outside its conventional application, here to resolve redox mechanisms. Consequently, it was possible to provide step-by-step identification of the reduction and oxidation pathways of iron in ferritin, and that the sequence of oxidation steps might not necessarily be preserved across ferritins. It was concluded for example that both 3-fold as well as 4-fold channels can have active roles in iron transfer. It was also posited that small, albeit targeted, differences in residues between ferritins can lead to significant changes in electrochemical and biochemical performances. Our work thus opens the door to more applied research where directed changes of specific residues could be used to increase performance of human ferritin when competition for iron resource and/or access to limited iron are conditions deemed to have critical health impact.

5.8 Experiments and methods

Sample preparation. All ferritin samples were obtained by expression in Escherichia coli and purification of the lysate using liquid chromatography following conventional protocols: Cloning and expression. The gene for ChF was obtained through amplification of Chaetopterus cDNA20 and cloned into the multiple cloning site of a pET24b vector using NdeI and BamHI restriction sites (using forward primer: CACAAGATCATATGGCCCAGACTCAGCCG and reverse primer: GTCGTGGATCCTTAGCTGCTCAGGCTCTCCTTGT). The gene for HuHF wild type was obtained through site directed mutagenesis of a codon optimized HuHF ΔC* mutant (in which all cysteines are replaced by alanine) in a pJexpress414 vector from DNA 2.0 (Menlo Park, CA) as previously described[130]. After transformation, BL21 star (Invitrogen) cultures were grown at 37 °C to an OD600nm of 0.7 - 0.8, induced with isopropyl β-D-1-thiogalactopyranoside (IPTG) and the proteins were expressed for 8 - 10 h after induction. The cells were harvested by centrifugation at 4,000 rcf for 25 mins at 4 °C. The cell pellet was resuspended in a 25 mM TRIS (tris(hydroxymethyl)aminomethane) buffer at pH 8.0 with 160 mM NaCl and lysed using lysozyme (Sigma) and Benzonase nuclease (EMD Millipore) at 37 °C for 30 min each, followed by sonication on ice for 3 min with 0.5 s intervals.

Purification. The resulting lysate was incubated in a warm water bath at 75 °C for 20 mins, followed by centrifugation at 4,000 rcf for 15 min to remove denatured protein. The remaining lysate was diluted in 25 mM TRIS buffer (pH 8.0) without NaCl and loaded onto a HisTrap Q HP column and eluted using a linearly increasing NaCl gradient. Of each collected fraction, 10 μL was tested for ferritin activity by adding 30 μL 2mM $FeCl_2$ and 120 μL MES buffer (20 mM MES, 200 mM NaCl, pH 6.85). After 20 minutes of incubation at room temperature, 20 μL FerroZine (1 mM) was added and all active samples (colorless or as determined by absorbance measurement at 562 nm in SpectraMax (Molecular Devices)) were pooled, concentrated in spin concentrators (Sartorius, molecular weight cut-off, MWCO: 50,000 Da) and further purified

through gel filtration on a Superdex 200 column in a 20 mM MOPS buffer with 150 mM NaCl at pH 6.5. All gel filtration fractions were also tested, and active fractions were selected and combined. All samples were further concentrated, and buffer exchanged to a Na_2HPO_4 buffer (50 mM Na_2HPO_4, 200 mM NaCl, pH 7.6) using spin concentrators with a MWCO of 50 kDa (Sartorius).

Iron determination. The average iron content of the ferritin cages was determined using Inductively Coupled Plasma Mass Spectrometry (ICP-MS). The protein samples used for DPV measurements were first diluted to around 1 mg/mL for protein determination by Bradford method. The 1 mg/mL samples were further diluted 100 times in 2% HNO_3 for the ICP-MS measurements. The Fe content was measured on an iCAPQc Single Quadrupole ICP-MS instrument (Thermo Fisher Scientific) with a 0.05 s dwell time and the analysis validated against the Fe content in a calibration series ranging from 1 to 1,000 ppb Fe standard, as routinely done in the elemental isotopic research facility (SIO). From these ICP-MS and Bradford measurements combined we obtained the total iron content per ferritin cage being between 8.5 and 10.5 Fe atoms for the WT samples before loading with FeCl2 (see Table S2 in Supplementary Information). Ferritin with slightly higher Fe content was prepared by adding 100 μL of 10 mM $FeCl_2$ to 1 mL ferritin solution of 20 mg/mL. Voltammetry was performed during loading as well as 48 hours after loading. The average load per ferritin cage at that point is estimated at 31-32 Fe per cage. Voltammetry measurements from native ferritin (10 Fe/cage average load) and slightly loaded ferritin (31-32 Fe/cage average load) showed identical peaks. For simplicity, the main text only shows results for the native ferritin.

Differential Pulse Voltammetry (DPV) and Interpretation. DPV was employed to probe the redox processes in solution and for obtaining high species-specific sensitivity35. Here, we probe the electrochemical characteristics of the ferritins (25 mg/mL with 9-10 Fe per cage), where the redox behavior is parameterized in terms of the relative abundance of the iron ion species (Fe2+ or Fe3+). The aim was to understand the performance of native ferritin (with 9-10

Fe per cage) and focus on the redox processes associated with the Fe only at the ferroxidase centers. The core ion related processes were not investigated, avoiding the complication of a large ferrihydrite core. Moreover, the Fe content (9-10 Fe/cage) gave results similar to what was observed with higher loading (with 31-32 Fe per cage) – as indicated in Section 4 of the Supplementary Information. As the DPV scans look similar to what was observed in the native ferritin case, i.e., Figures S5 in the Supplementary Information, we deem our native ferritin-based experiments to be representative of the redox processes and mechanisms indicated here. The background electrolyte was a phosphate buffer (pH 7.6) and 0.2 M NaCl to keep a moderate ionic strength[67] and to guarantee stability and activity of the enzyme21. The ferritins (as also discussed in the previous section) were interrogated through suspension in the electrolyte, in the absence of background chelators, with a glassy carbon electrode (GCE), which served as the working electrode. A Pt wire and a saturated calomel electrode (SCE) functioned as the counter electrode and the reference electrode, respectively. An electrical current peak, in response to a voltage pulse, is a measure of the Faradic response of the ferritin, and probes both iron reduction (/oxidation) in cathodic (/anodic), with decreasing (/increasing) applied voltages. This voltammetric measurement incorporates the application of a voltage pulse (of typical magnitude V_p of 50 mV, and applied for 100 ms, in our experiments), superposed on a steadily increasing base voltage (Vbase). Step size was selected as 2 mV and sample period was 1 s. The difference in the electrical current before and after the voltage pulse is recorded and is a measure of the Faradic response. The V_{base} is increased from below the redox potential (E_{redox}) to a larger value; at lower voltages, inadequate Faradic processes result in a low sampled current, while at voltages larger than Eredox, the current is diffusion limited and low. In the intermediate regime, an electrical current peak is manifested corresponding to the relevant redox reaction. Moreover, taking the difference of the electrical currents at relatively close values of the voltage in a time interval, ensures adequate subtraction of the background contributions. Consideration of the attributes such as the (i) ratio of the peak Anodic current (ipA) to the peak Cathodic current (ip_C),

(ii) the respective half-peak widths ($W^{A}_{1/2}$ and $W^{C}_{1/2}$), (iii) the separation: ΔEp (= $|Ep_A - Ep_C|$) between the anodic peak voltage (Ep_A) and the cathodic peak voltage (Ep_C), have been used to indicate the electrochemical kinetics and related mechanisms[24, 26]. An ip_A/ip_C ratio closer to unity imply a reversible, single-electron transfer, electrochemical (E) process, while a ratio less (/more) than unity connotes an underlying EC (/CE) mechanism, where the following (/preceding) C indicates a chemically coupled electron transfer process.[4, 5, 25], for instance, as in leading to iron storage compound formation. Correspondingly, a $W^{A}_{1/2}/W^{C}_{1/2}$ ratio equal to unity implies E processes, while a ratio more (/less) than unity posits an EC (/CE) mechanism[26, 132]. Such analyses probe new frontiers in ferritin protein function, yielding insights into related electron transfer mechanism.

5.9 Acknowledgement

The authors are grateful for support from the National Science Foundation (NSF: CBET 1606192, to P.R.B.) and from the Air Force Office of Scientific Research (AFOSR FA9550-17-0189, to D.D.D.). We acknowledge Prof. J. Day at the Scripps Isotope Geochemistry Laboratory for performing the ICP-MS measurements.

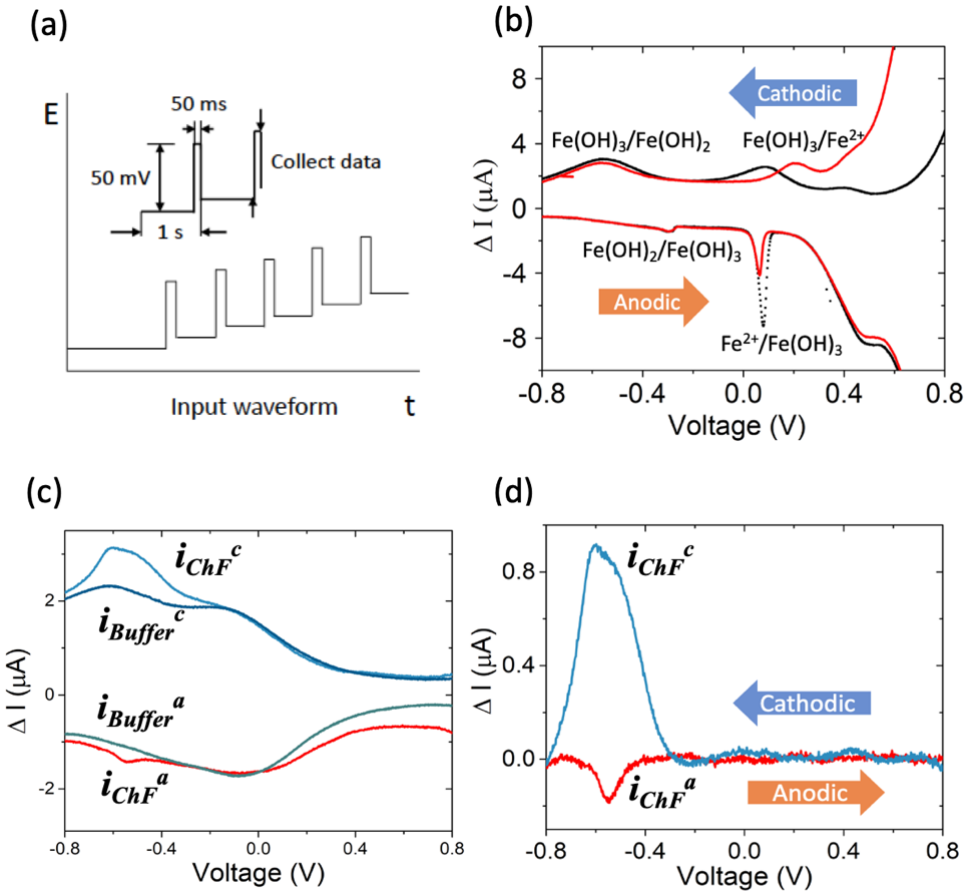

Figure 5.5: Differential pulse voltammetry (DPV) was used for the interrogation of the redox characteristics of the ferritin and incorporates (a) the application of a voltage pulse (of typical magnitude V_p of 50 mV, and applied for 100 ms, in our experiments), superposed on a steadily increasing base voltage (V_{base}). The difference in the electrical current before and after the voltage pulse is a measure of the Faradic response of the ferritin and is manifested through an electrical current peak corresponding to the relevant redox (reduction/oxidation) reactions.(b) DPV scans of $FeCl_2$ in aqueous solution. Black, pH 7, and Red, pH 14. The redox peaks, observed in the cathodic scan, correspond broadly to the $Fe^{3+} \rightarrow Fe^{2+}$ reduction processes, and related to the $Fe(OH)_3/Fe(OH)_2$. In the reverse voltage scan, anodic redox peaks arise from the $Fe^{2+} \rightarrow Fe^{3+}$ oxidation processes, and are related to the $Fe^{2+}/Fe(OH)_3$ (c) A comparative DPV with cathodic (c) and anodic (a) scans of ChF (in a phosphate buffer and NaCl) – outer curves, and the Buffer (without ChF) – inner curves. The subtraction of the Buffer scans from the observed signals from the combined ChF + Buffer yield a clearer delineation of the peaks belonging to the ChF alone. (d) Same raw data as from panel (c) but after Buffer background signal subtraction. This last format is how voltammograms will be presented in the remaining of this work.

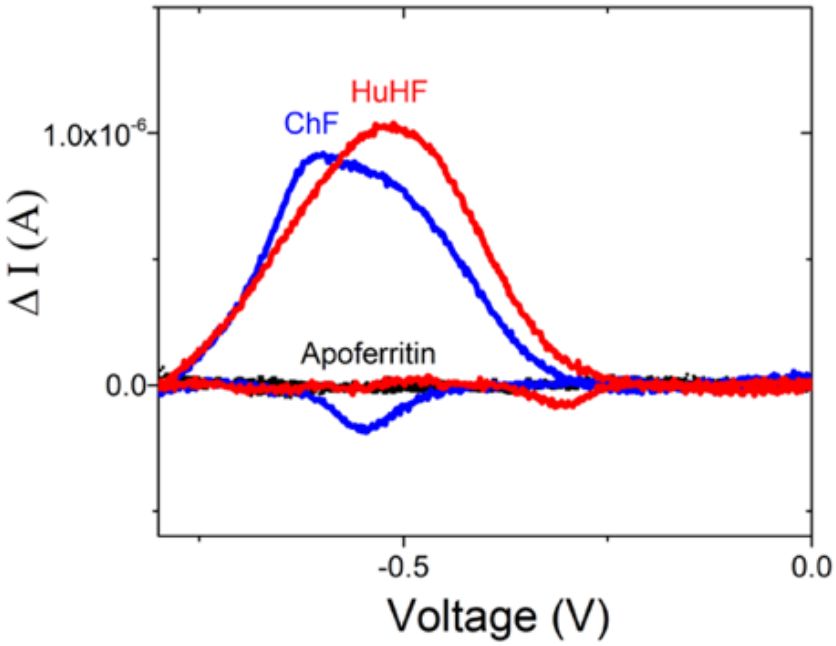

Figure 5.6: Comparison of the DPV spectra of HuHF (red), ChF (blue) and Apoferritin (black)

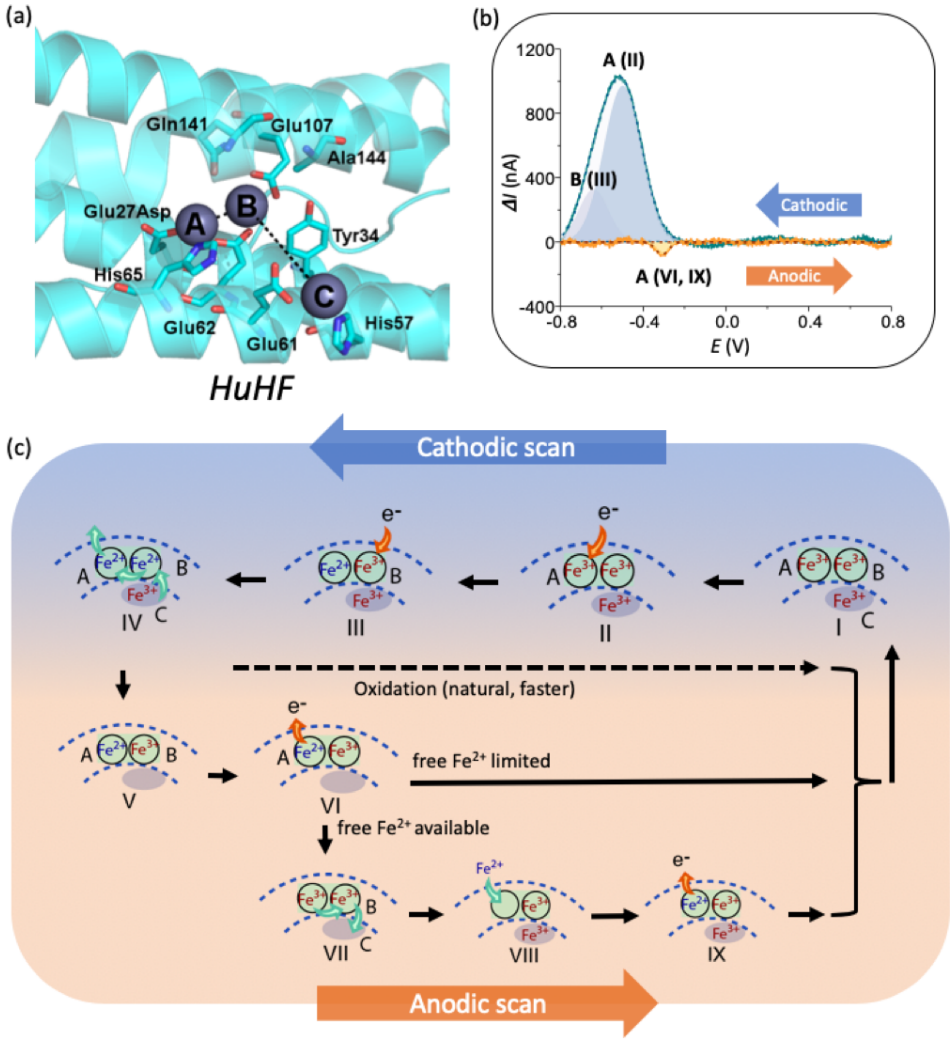

Figure 5.7: Redox kinetics in HuHF probed through differential pulse voltammetry and proposed redox mechanisms. (a) The HuHF ferroxidase center within a single subunit, indicating key residues and A, B and C sites. The respective distances between the metal ions are: A-B 3.5 Å, B-C 9.2 Å. PyMol14 was used to visualize HuHF with Zn in all 3 sites from 2CIH.pdb, despite the Glu27Asp mutation, (b) DPV derived peaks for HuHF, cathodic scan read first. The cathodic peak may be deconvolved to yield two contributions, related to the A and B sites of the ferritin, respectively, and the anodic peak is paired to the A peak. Roman numerals refer to relevant processes depicted in (c) - proposed mechanism for charge transfer processes in HuHF, as derived from the measured voltammograms.

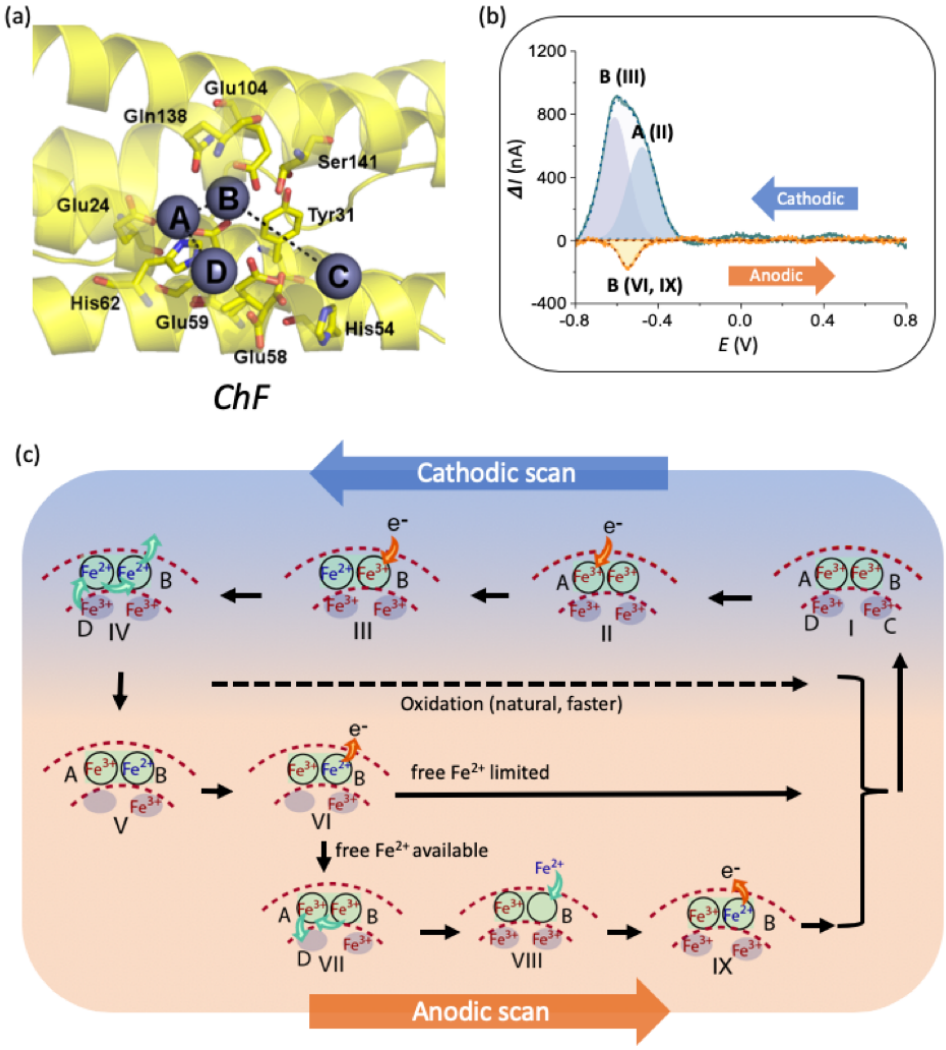

Figure 5.8: Redox kinetics in Chaetopterus ferritin (ChF) probed through differential pulse voltammetry and proposed iron redox mechanisms. (a) The ferroxidase center structure in ChF, showing all key residues including Ser141. The respective distances between the metal ions are: D-A 6.3 Å, A-B 3.4 Å, B-C 9.3 Å. ChF structure shown from 5WPN.pdb and visualized in PyMol14. An additional metal binding site near the ferroxidase center is found in 5WPN and labeled as site D. (b) DPV derived peaks for ChF, in the cathodic and anodic scans. The cathodic peak is deconvolved to yield contributions related to the A and B sites of the ferritin. The anodic oxidation peak is associated with the B peak only. (c) The hypothesized mechanism for the charge transfer processes related to the Fe redox kinetics in ChF based on the DPV scan.

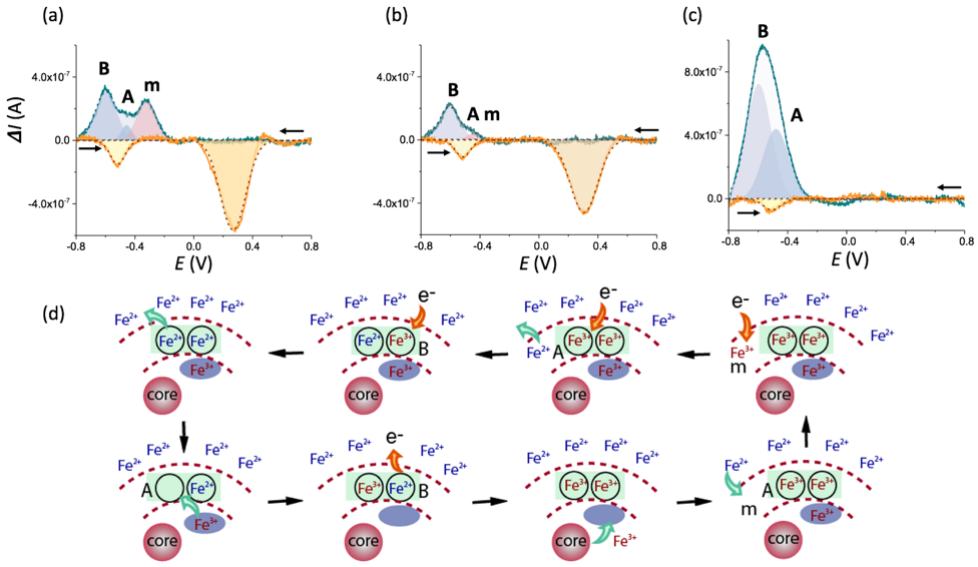

Figure 5.9: The dynamics of iron uptake and release in ChF, as a function of time - (a) with analyzed an ipA/ipC ratio of 0.8 and a W1/2A/W1/2C ratio of 1.2; 2 hours later - (b) with ip_A/ip_C ratio of 0.8 and a $W^A_{1/2}/W^C_{1/2}$ ratio of 1.2 and 48 hours later - (c), to yield an ip_A/ip_C ratio of 0.4 and a $W^A_{1/2}/W^C_{1/2}$ ratio of 2.7. Schematic representation of the charge transfer process during iron loading (d) inside ferritin subunit. A new iron site labeled as m is shown in this diagram. In this scheme, adequate amount of free Fe^{2+} ions exist external to ferritin shell.

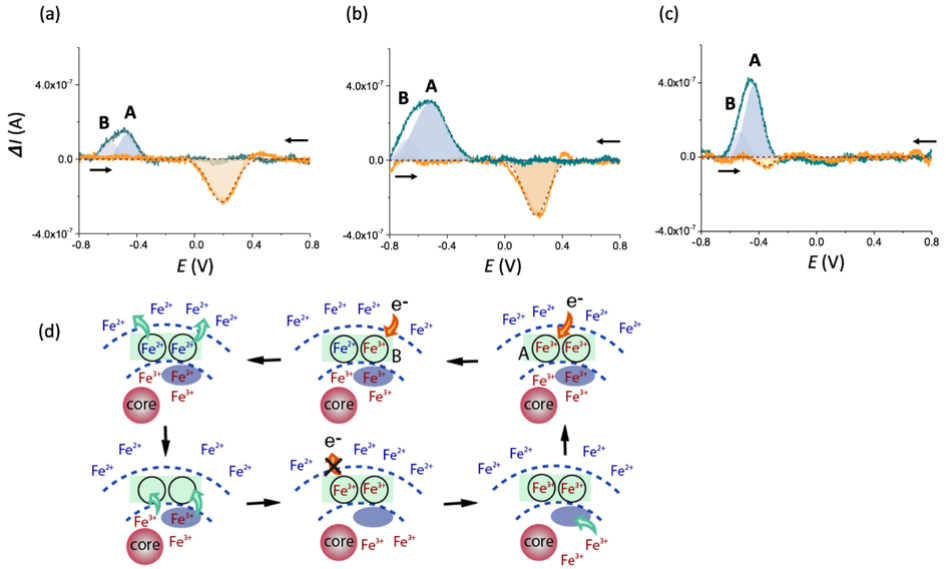

Figure 5.10: The dynamics of iron uptake and release in HuHF, as a function of time, considering both cathodic (top) and anodic (bottom) processes at the time of loading - (a), 2 hours later – (b), and 48 hours later - (c), yielding an ip_A/ip_C ratio 0.4 and a $W^A_{1/2}/W^C_{1/2}$ ratio of 2.6; Schematic representation of the charge transfer process during iron loading (d) inside ferritin subunit. In this scheme, adequate amount of free Fe^{2+} ions exist external to ferritin shell.

Chapter 6

Conclusion and Future Work

6.1 Conclusion

In summary, we have indicated the crucial role of non-stoichiometry in oxides for enhanced photoelectrochemical current density, using WO_{3-x} as a prototype. Given that OER proceeds through the interaction of hole charge carriers (h^+) with water and that the presence of h^+ implies surface instability, we indicate that a charge compensating mechanism through electrons from oxygen vacancies[82] may be beneficial. Indeed, we found that a critical vacancy and h^+ concentration, increases the photoelectrochemical performance. The accumulation of h^+ at the surface over a distance of the diffusion length to accomplish band bending for enhanced kinetics is also posited. It is hoped that the consideration of such defect engineering[65, 66] aspects, perhaps at the atomic level[13], would be helpful in designing higher efficiency electrodes for water oxidation[66].

Our work also indicates that surface engineering through helium plasma bombardment is a viable technique for modulating the charging characteristics of metal surfaces. It was shown here that it would be possible to significantly alter the charge states, e.g., through modulating the PZC, as well as the kinetics of charge transfer, e.g., as manifested in the variation with respect

to the voltage cycling rate, through surface modification. It was also shown that contact angle modulations could be transduced into the relative changes of the surface potential and charge density. While the rate constants could provide one measure for the observations, more detailed interpretation requires detailed knowledge of the local chemical equilibria as well as physical attributes related to local curvature and roughness. The present work, supplemented by such investigations would be of much utility in exploring further the electrical interface[111] at the electrodes with implications to enhancing the capacitance as well as the charge capacity and energy storage.

The ferritin chapter yields considerable insight related to the molecular mechanisms of ferroxidase activity in ferritins. The benefit of integrating analyses for tailored biochemical performances across different animal species was demonstrated, where ferritin operates under different environmental constraints, through DPV - which for the first time was used outside its conventional application, here to resolve redox mechanisms. Consequently, it was possible to provide step-by-step identification of the reduction and oxidation pathways of iron in ferritin, and that the sequence of oxidation steps might not necessarily be preserved across ferritins. It was concluded for example that both 3-fold as well as 4-fold channels can have active roles in iron transfer. It was also posited that small, albeit targeted, differences in residues between ferritins can lead to significant changes in electrochemical and biochemical performances. Our work thus opens the door to more applied research where directed changes of specific residues could be used to increase performance of human ferritin when competition for iron resource and/or access to limited iron are conditions deemed to have critical health impact.

6.2 Future work

The distinct phenomenon observed in fuzzy tungsten enlightens possible researches on tungsten based electronic device. Since the movement of charged vacancies can be triggered

under external bias, oxygen vacancies as well as the conductivity of tungsten oxide can be tuned with applied voltage. This unique property enables oxygen deficient tungsten oxide as a candidate for Resistive Random Access Memory (RRAM). In the aspect of PEC applications, starting with an extraordinary stability of semiconductor material, it's easier to follow-up catalyst study to enhance light absorption efficiency. Another direction is the recycle possibility of tungsten oxide. With a simple compound component and tunable oxygen level in tungsten, we would consider if we can reuse the material under simple oxidation process/ when the top oxide layer gets corroded.

For the ferritin study, we have two directions to put efforts: 1. DPV shows advantages to investigating iron release process in ferritin, more experiments can be conducted on loaded iron to have a dynamic picture of iron delivery process. By loading iron, iron mediate state would give distinct current signal on voltammetry, which can be an entry point to reveal iron pathway/intermediate states across different animal species. The potential shift also indicates the energy consumption in iron uptake/release process which can be quantified with thermodynamic study. 2. Based on the DPV methodology, we can further couple electrochemical analyses and optical experiments. The idea is to trigger charge transfer via transient current at redox potential and detect possible photo emission with photodetector. The purpose of this study is to detect the direct correlation between charge transfer process and light emission.

Chapter 7

Bibliography

Bibliography

[1] A. J. Nozik and R. Memming, "Physical chemistry of semiconductor-liquid interfaces," *The Journal of Physical Chemistry*, vol. 100, no. 31, pp. 13061–13078, 1996.

[2] R. Rawat and D. D. Deheyn, "Evidence that ferritin is associated with light production in the mucus of the marine worm Chaetopterus," *Scientific Reports*, vol. 6, p. 36854, 2016.

[3] E. De Meulenaere, J. B. Bailey, F. A. Tezcan, and D. D. Deheyn, "First biochemical and crystallographic characterization of a fast-performing ferritin from a marine invertebrate.," *The Biochemical journal*, p. BCJ20170681, 2017.

[4] C. Léger and P. Bertrand, "Direct electrochemistry of redox enzymes as a tool for mechanistic studies," 2008.

[5] C. Léger, S. J. Elliott, K. R. Hoke, L. J. C. Jeuken, A. K. Jones, and F. A. Armstrong, "Enzyme electrokinetics: Using protein film voltammetry to investigate redox enzymes and their mechanisms," 2003.

[6] S. Chen and L.-W. Wang, "Thermodynamic oxidation and reduction potentials of photocatalytic semiconductors in aqueous solution," *Chemistry of Materials*, vol. 24, no. 18, pp. 3659–3666, 2012.

[7] B. Klahr, S. Gimenez, F. Fabregat-Santiago, T. Hamann, and J. Bisquert, "Water Oxidation

at Hematite Photoelectrodes: The Role of Surface States," *Journal of the American Chemical Society*, vol. 134, pp. 4294–4302, mar 2012.

[8] T. Zhu, M. N. Chong, and E. S. Chan, "Nanostructured Tungsten Trioxide Thin Films Synthesized for Photoelectrocatalytic Water Oxidation: A review," *ChemSusChem*, vol. 7, pp. 2974–2997, nov 2014.

[9] H. Zheng, J. Z. Ou, M. S. Strano, R. B. Kaner, A. Mitchell, and K. Kalantar-zadeh, "Nanostructured Tungsten Oxide - Properties, Synthesis, and Applications," *Advanced Functional Materials*, vol. 21, pp. 2175–2196, jun 2011.

[10] G. Wang, Y. Ling, H. Wang, X. Yang, C. Wang, J. Z. Zhang, and Y. Li, "Hydrogen-treated WO3 nanoflakes show enhanced photostability," *Energy & Environmental Science*, vol. 5, no. 3, p. 6180, 2012.

[11] J. Yan, T. Wang, G. Wu, W. Dai, N. Guan, L. Li, and J. Gong, "Tungsten Oxide Single Crystal Nanosheets for Enhanced Multichannel Solar Light Harvesting," *Advanced Materials*, vol. 27, pp. 1580–1586, 2015.

[12] J. Greeley and N. Markovic, "The road from animal electricity to green energy; combining experiment and theory in electrocatalysis," *Energy and Environmental Science*, vol. 5, p. 9246, 2012.

[13] Y. Li, P. Liu, L. Pan, H. Wang, Z. Yang, L. Zheng, P. Hu, H. Zhao, L. Gu, and H. Yang, "Local atomic structure modulations activate metal oxide as electrocatalyst for hydrogen evolution in acidic water," *Nature Communications*, vol. 6, p. 8064, 2015.

[14] R. Navarro, F. del Valle, J. Villoria de la Mano, M. Álvarez-Galván, and J. Fierro, "Photocatalytic Water Splitting Under Visible Light," in *Advances in Chemical Engineering*, vol. 36, pp. 111–143, Elsevier, 2009.

[15] T. Hisatomi, J. Kubota, and K. Domen, "Recent advances in semiconductors for photocatalytic and photoelectrochemical water splitting," *Chemical Society Reviews*, vol. 43, no. 22, pp. 7520–7535, 2014.

[16] K. Huang and Q. Zhang, "Giant persistent photoconductivity of the wo 3 nanowires in vacuum condition," *Nanoscale Res Lett*, vol. 6, no. 1, p. 52, 2011.

[17] J.-M. Savéant, *Elements of Molecular and Biomolecular Electrochemistry*. Hoboken, NJ, USA: John Wiley & Sons, Inc., jan 2006.

[18] G. D. Watt, D. Jacobs, and R. B. Frankel, "Redox reactivity of bacterial and mammalian ferritin: is reductant entry into the ferritin interior a necessary step for iron release?," *Proceedings of the National Academy of Sciences of the United States of America*, vol. 85, pp. 7457–61, oct 1988.

[19] R. J. Cherry, A. J. Bjornsen, and D. C. Zapien, "Direct Electron Transfer of Ferritin Adsorbed at Tin-Doped Indium Oxide Electrodes," *Langmuir*, vol. 14, no. 8, pp. 1971–1973, 1998.

[20] M.-S. Pyon, R. Cherry, A. Bjornsen, and D. Zapien, "Uptake and Release of Iron by Ferritin Adsorbed at Tin-Doped Indium Oxide Electrodes," *Langmuir*, vol. 15, pp. 7040–7046, 1999.

[21] D. C. Zapien and M. A. Johnson, "Direct electron transfer of ferritin adsorbed at bare gold electrodes," *Journal of Electroanalytical Chemistry*, vol. 494, pp. 114–120, dec 2000.

[22] X. Yang, Y. Chen-Barrett, P. Arosio, and N. D. Chasteen, "Reaction paths of iron oxidation and hydrolysis in horse spleen and recombinant human ferritins," *Biochemistry*, vol. 37, no. 27, pp. 9743–9750, 1998.

[23] L. J. Jeuken, "Biophotoelectrochemistry : from bioelectrochemistry to biophotovoltaics.," vol. 158, 2017.

[24] A. J. Bard and L. R. Faulkner, *Electrochemical methods : fundamentals and applications*. Wiley, 2001.

[25] J. Hirst and F. A. Armstrong, "Fast-scan cyclic voltammetry of protein films on pyrolytic graphite edge electrodes: Characteristics of electron exchange," *Analytical Chemistry*, vol. 70, no. 23, pp. 5062–5071, 1998.

[26] M. H. Kim, L. Yan, R. L. Birke, and M. Z. Czae, "Differential Pulse Polarography for a First-Order EC Process and Its Diagnostic Parameters," *Electroanalysis*, vol. 15, no. 19, pp. 1541–1553, 2003.

[27] H. Heering, J. Hirst, and F. Armstrong, "Interpreting the catalytic voltammetry of electroactive enzymes adsorbed on electrodes," *Journal of Physical Chemistry B*, vol. 102, pp. 6889–6902, 1998.

[28] K. Honarmand Ebrahimi, P. L. Hagedoorn, and W. R. Hagen, "Unity in the biochemistry of the iron-storage proteins ferritin and bacterioferritin," jan 2015.

[29] A. Marchetti, M. Parker, L. Moccia, E. Lin, A. Arrieta, F. Ribalet, M. Murphy, M. Maldonado, and E. Armbrust, "Ferritin is used for the iron storage in bloom-forming marine pennate diatoms," *Nature*, vol. 457, p. 467, 2009.

[30] X. Liu and E. Theil, "Ferritins: Dynamic Management of Biological Iron and Oxygen Chemistry," *Accounts of Chemical Research*, vol. 38, pp. 167–175, 2005.

[31] F. Bou-Abdallah, "The iron redox and hydrolysis chemistry of the ferritins," *Biochimica et Biophysica Acta (BBA) - General Subjects*, vol. 1800, pp. 719–731, aug 2010.

[32] K. Honarmand Ebrahimi, E. Bill, P.-L. P.-L. Hagedoorn, W. W. R. Hagen, K. Ebrahimi, E. Bill, P.-L. P.-L. Hagedoorn, and W. W. R. Hagen, "The catalytic center of ferritin regulates iron storage via Fe(II)-Fe(III) displacement," *Nature Chemical Biology*, vol. 8, no. 11, pp. 941–948, 2012.

[33] R. Laghaei, W. Kowallis, D. G. Evans, and R. D. Coalson, "Calculation of iron transport through human H-chain ferritin," *Journal of Physical Chemistry A*, vol. 118, pp. 7442–7453, sep 2014.

[34] F. Bou-Abdallah, G. Zhao, G. Biasiotto, M. Poli, P. Arosio, and N. D. Chasteen, "Facilitated Diffusion of Iron(II) and Dioxygen Substrates into Human H-Chain Ferritin. A Fluorescence and Absorbance Study Employing the Ferroxidase Center Substitution Y34W," *Journal of the American Chemical Society*, vol. 130, pp. 17801–17811, dec 2008.

[35] R. K. Behera and E. C. Theil, "Moving Fe2+ from ferritin ion channels to catalytic OH centers depends on conserved protein cage carboxylates.," *Proceedings of the National Academy of Sciences of the United States of America*, vol. 111, pp. 7925–30, jun 2014.

[36] M. H. Kim and R. L. Birke, "Differential pulse polarography for a first-order catalytic process," *Analytical Chemistry*, vol. 55, no. 3, pp. 522–527, 2002.

[37] A. Fujishima and K. Honda, "Electrochemical Photolysis of Water at a Semiconductor Electrode," *Nature*, vol. 238, pp. 37–38, jul 1972.

[38] M. Boxwell, *The Solar Electricity Handbook - 2016 Edition: A simple, practical guide to solar energy: how to design and install photovoltaic solar electric systems*. Greenstream Publishing, 2016.

[39] H. Ghasemi, G. Ni, A. M. Marconnet, J. Loomis, S. Yerci, N. Miljkovic, and G. Chen, "Solar steam generation by heat localization.," *Nature communications*, vol. 5, p. 4449, jan 2014.

[40] M. Grätzel, "Solar energy conversion by dye-sensitized photovoltaic cells.," *Inorganic chemistry*, vol. 44, pp. 6841–51, oct 2005.

[41] T. M. Tritt, H. Böttner, and L. Chen, "Thermoelectrics: Direct Solar Thermal Energy Conversion," *MRS Bulletin*, vol. 33, no. 4, pp. 366–368, 2008.

[42] M. Thirugnanasambandam, S. Iniyan, and R. Goic, "A review of solar thermal technologies," *Renewable and Sustainable Energy Reviews*, vol. 14, pp. 312–322, jan 2010.

[43] K. Sampathkumar, T. Arjunan, P. Pitchandi, and P. Senthilkumar, "Active solar distillation A detailed review," *Renewable and Sustainable Energy Reviews*, vol. 14, pp. 1503–1526, aug 2010.

[44] N. S. Lewis, "Research opportunities to advance solar energy utilization," *Science*, vol. 351, pp. aad1920–aad1920, jan 2016.

[45] M. T. Koper, "Thermodynamic theory of multi-electron transfer reactions: Implications for electrocatalysis," *Journal of Electroanalytical Chemistry*, vol. 660, no. 2, pp. 254–260, 2011.

[46] E. Fabbri, A. Habereder, K. Waltar, R. Kotz, and T. J. Schmidt, "Developments and perspectives of oxide-based catalysts for the oxygen evolution reaction," *Catal. Sci. Technol.*, vol. 4, pp. 3800–3821, 2014.

[47] L. Trotochaud, S. L. Young, J. K. Ranney, and S. W. Boettcher, "Nickel-Iron Oxyhydroxide Oxygen-Evolution Electrocatalysts: The Role of Intentional and Incidental Iron Incorporation," *Journal of the American Chemical Society*, vol. 136, pp. 6744–6753, may 2014.

[48] P. Dias, A. Vilanova, T. Lopes, L. Andrade, and A. Mendes, "Extremely stable bare hematite photoanode for solar water splitting," *Nano Energy*, vol. 23, pp. 70–79, 2016.

[49] K. Sivula, F. Le Formal, and M. Gratzel, "Solar Water Splitting: Progress Using Hematite (α-Fe2O3) Photoelectrodes," *ChemSusChem*, vol. 4, pp. 432–449, apr 2011.

[50] L. C. Seitz, C. F. Dickens, K. Nishio, Y. Hikita, J. Montoya, A. Doyle, C. Kirk, A. Vojvodic, H. Y. Hwang, J. K. Norskov, and T. F. Jaramillo, "A highly active and stable IrOx/SrIrO3 catalyst for the oxygen evolution reaction," *Science*, vol. 353, pp. 1011–1014, sep 2016.

[51] Z.-F. Huang, J. Song, L. Pan, X. Zhang, L. Wang, and J.-J. Zou, "Tungsten Oxides for Photocatalysis, Electrochemistry, and Phototherapy," *Advanced Materials*, vol. 27, pp. 5309–5327, 2015.

[52] S. Yoon, E. Kang, J. Kim, C. Lee, and J. Lee, "Development of high-performance supercapacitor electrodes using novel ordered mesoporous tungsten oxide materials with high electrical conductivity," *Chemical Communications*, vol. 47, pp. 1021–1023, 2011.

[53] J. M. Berak and M. Sienko, "Effect of oxygen-deficiency on electrical transport properties of tungsten trioxide crystals," *Journal of Solid State Chemistry*, vol. 2, no. 1, pp. 109–133, 1970.

[54] S. Jeon and K. Yong, "Morphology-controlled synthesis of highly adsorptive tungsten oxide nanostructures and their application to water treatment," *Journal of Materials Chemistry*, vol. 20, pp. 10146–10151, 2010.

[55] H. Zheng, J. Z. Ou, M. S. Strano, R. B. Kaner, A. Mitchell, and K. Kalantar-zadeh, "Nanostructured tungsten oxide–properties, synthesis, and applications," *Advanced Functional Materials*, vol. 21, no. 12, pp. 2175–2196, 2011.

[56] W. Li, P. Da, Y. Zhang, Y. Wang, X. Lin, X. Gong, and G. Zheng, "WO ₃ Nanoflakes for Enhanced Photoelectrochemical Conversion," *ACS Nano*, vol. 8, pp. 11770–11777, nov 2014.

[57] D. Goebel, G. Campbell, and R. Conn, "Plasma surface interaction experimental facility (PISCES) for materials and edge physics studies," *Journal of Nuclear Materials*, vol. 121, pp. 277–282, may 1984.

[58] M. Baldwin and R. Doerner, "Formation of helium induced nanostructure 'fuzz' on various tungsten grades," *Journal of Nuclear Materials*, vol. 404, pp. 165–173, sep 2010.

[59] M. de Respinis, G. De Temmerman, I. Tanyeli, M. C. van de Sanden, R. P. Doerner, M. J. Baldwin, and R. van de Krol, "Efficient Plasma Route to Nanostructure Materials: Case Study on the Use of m-WO ₃ for Solar Water Splitting," *ACS Applied Materials & Interfaces*, vol. 5, pp. 7621–7625, aug 2013.

[60] S. Kajita, N. Yoshida, N. Ohno, and Y. Tsuji, "Growth of multifractal tungsten nanostructure by He bubble induced directional swelling," *New Journal of Physics*, vol. 17, p. 043038, 2015.

[61] H. Fan, Z. Wu, T. Sun, M. Yang, J. Guo, K. Yang, and Y. Li, "Efficient plasma-assisted approach in nanostructure fabrication of tungsten," *Materials & Design*, vol. 89, pp. 78–84, 2016.

[62] G. Gu, B. Zheng, W. Han, S. Roth, and J. Liu, "Tungsten Oxide Nanowires on Tungsten Substrates," *Nanoletters*, vol. 2, pp. 849–851, 2002.

[63] T. He and J. Yao, "Photochromic materials based on tungsten oxide," *Journal of Materials Chemistry*, vol. 17, pp. 4547–4557, 2007.

[64] S. Baeck, T. F. Jaramillo, G. D. Stucky, and E. McFarland, "Controlled Electrodeposition of Nanoparticulate Tungsten Oxide," *Nanoletters*, vol. 2, pp. 831–834, 2002.

[65] N. Zhang, X. Li, H. Ye, S. Chen, H. Ju, D. Liu, Y. Lin, W. Ye, C. Wang, Q. Xu, J. Zhu, L. Song, J. Jiang, and Y. Xiong, "Oxide Defect Engineering Enables to Couple Solar

Energy into Oxygen Activation," *Journal of the American Chemical Society*, vol. 138, pp. 8928–8935, 2016.

[66] Y. Li, Z. Tang, J. Zhang, and Z. Zhang, "Defect engineering of air-treated WO3 and its enhanced visible-light-driven photocatalytic and electrochemical performance," *Journal of Physical Chemistry C*, vol. 120, pp. 9750–9753, 2016.

[67] R. G. Compton and C. E. Banks, *Understanding Voltammetry*. London: Imperial College Press, 2011.

[68] D. G. Leaist, "Diffusion in aqueous solutions of sulfuric acid," *Canadian Journal of Chemistry*, vol. 62, pp. 1692–1697, sep 1984.

[69] J. W. Mullin and A. W. Nienow, "Diffusion Coefficients of Potassium Sulfate in Water.," *Journal of Chemical & Engineering Data*, vol. 9, pp. 526–527, oct 1964.

[70] F. Wang, C. D. Valentin, and G. Pacchioni, "Semiconductor-to-metal transition in WO3-x : Nature of the oxygen vacancy," *Physical Review B*, vol. 84, p. 073103, 2011.

[71] P. H. Rieger, *Electrochemistry*. New York: Chapman and Hall, 2 ed., 1994.

[72] D. M. Pozar, *Microwave engineering*. Hoboken: Wiley, 4th ed ed., 2012.

[73] A. Polaczek, M. Pekala, and Z. Obuszko, "Magnetic susceptibility and thermoelectric power of tungsten intermediary oxides," *Journal of Physics: Condensed Matter*, vol. 6, p. 7909, sep 1994.

[74] R. S. Muller and T. I. Kamins, *Device Electronics for Integrated Circuits*. New York: John Wiley, 2 ed., 1986.

[75] W. Wang, A. Janotti, and C. G. Van de Walle, "Role of oxygen vacancies in crystalline WO3," *Journal of Materials Chemistry, C*, vol. 4, no. 6641-6648, 2016.

[76] M. Mews, L. Korte, and B. Rech, "Oxygen vacancies in tungsten oxide and their influence on tungsten oxide/silicon heterojunction solar cells," *Solar Energy Materials and Solar Cells*, vol. 158, pp. 77–83, 2016.

[77] F. Wang, C. Di Valentin, and G. Pacchioni, "Semiconductor-to-metal transition in wo 3- x: Nature of the oxygen vacancy," *Physical Review B*, vol. 84, no. 7, p. 073103, 2011.

[78] M. Gillet, C. Lemire, E. Gillet, and K. Aguir, "The role of surface oxygen vacancies upon WO3 conductivity," *Surface Science*, vol. 532-535, pp. 519–525, 2003.

[79] H. Le, N. Vu, and B.-T. Phan, "Migrations of oxygen vacancy in tungsten oxide (WO3): A density functional theory study," *Computational Materials Science*, vol. 90, pp. 171–176, 2014.

[80] C.-F. Sun, H. Zhu, M. Okada, K. Gaskell, Y. Inoue, L. Hu, and Y. Wang, "Interfacial Oxygen Stabilizes Composite Silicon Anodes," *Nanoletters*, vol. 15, pp. 703–708, 2015.

[81] R. Chandrasena, W. Yang, Q. Lei, M. Delgado-Jaime, K. Wijesekara, M. Golalikhani, B. Davidson, E. Arenholz, K. Kobayashi, M. Kobata, F. de Groot, U. Aschauer, N. Spaldin, X. Xi, and A. Gray, "Strain-Engineered Oxygen Vacancies in CaMnO3 Thin Films," *Nanoletters*, vol. 17, pp. 794–799, 2017.

[82] Z.-P. Nie, D.-K. Ma, G.-Y. Fang, W. Chen, and S.-M. Huang, "Concave Bi2WO6 nanoplates with oxygen vacancies achieving enhanced electrocatalytic oxygen evolution in near-neutral water," *Journal of Materials Chemistry A*, vol. 4, pp. 2438–2444, 2016.

[83] P. B. Ishai, M. S. Talary, A. Caduff, E. Levy, and Y. Feldman, "Electrode polarization in dielectric measurements: A review," 2013.

[84] P. Delahay, *Double Layer and Electrode Kinetics*. New York: Interscience, 1965.

[85] L. Vitos, A. Ruban, H. Skriver, and J. Kollar, "The surface energy of metals," *Surface Science*, vol. 411, pp. 186–202, 1998.

[86] S. Kajita, W. Sakaguchi, N. Ohno, N. Yoshida, and T. Saeki, "Formation process of tungsten nanostructure by the exposure to helium plasma under fusion relevant plasma conditions," *Nuclear Fusion*, vol. 49, p. 095005, 2009.

[87] T. J. Petty, A. Khan, T. Heil, and J. W. Bradley, "Fuzzy tungsten in a magnetron sputtering device," *Journal of Nuclear Materials*, vol. 480, pp. 374–385, nov 2016.

[88] M. Grätzel, "Solar energy conversion by dye-sensitized photovoltaic cells," *Inorganic chemistry*, vol. 44, no. 20, pp. 6841–6851, 2005.

[89] P. Chen, M. Baldwin, and P. R. Bandaru, "Hierarchically structured, oxygen deficient, tungsten oxide morphologies for enhanced photoelectrochemical charge transfer and stability," *Journal of Materials Chemistry A*, vol. 5, pp. 14898–14905, jul 2017.

[90] B. Reichman and A. J. Bard, "The Electrochromic Process at WO[sub 3] Electrodes Prepared by Vacuum Evaporation and Anodic Oxidation of W," *Journal of The Electrochemical Society*, vol. 126, p. 583, apr 1979.

[91] D. Y. Chan and D. Mitchell, "The free energy of an electrical double layer," *Journal of Colloid and Interface Science*, vol. 95, pp. 193–197, sep 1983.

[92] A. Di Paola, F. D. Quarto, and C. Sunseri, "Electrochromism in Anodically Formed Tungsten Oxide Films," *Journal of The Electrochemical Society*, vol. 125, p. 1344, aug 1978.

[93] P. Ortiz, M. Teijelo, and M. Giordano, "Electrochemical behaviour of tungsten in alkaline media: Part I. NaOH solutions," *Journal of Electroanalytical Chemistry and Interfacial Electrochemistry*, vol. 243, pp. 379–391, mar 1988.

[94] R. Armstrong, K. Edmondson, and R. Firman, "The anodic dissolution of tungsten in alkaline solution," *Journal of Electroanalytical Chemistry and Interfacial Electrochemistry*, vol. 40, pp. 19–28, nov 1972.

[95] T. Heumann and N. Stolica, "The electrochemical behaviour of tungsten I. The dissolution of tungsten and tungsten oxides in buffer solutions," *Electrochimica Acta*, vol. 16, pp. 643–651, may 1971.

[96] S. Takamura, N. Ohno, D. Nishijima, and S. Kajita, "Formation of Nanostructured Tungsten with Arborescent Shape due to Helium Plasma Irradiation," *Plasma and Fusion Research*, vol. 1, p. 051, 2006.

[97] M. Baldwin and R. Doerner, "Helium induced nanoscopic morphology on tungsten under fusion relevant plasma conditions," *Nuclear Fusion*, vol. 48, p. 035001, 2008.

[98] S. Krasheninnikov, "Viscoelastic model of tungsten 'fuzz' growth," *Physics Scripta*, vol. T145, p. 014040, 2011.

[99] R. Narayanan and P. R. Bandaru, "High Rate Capacity through Redox Electrolytes Confined in Macroporous Electrodes," *Journal of The Electrochemical Society*, vol. 162, no. 1, pp. A86–A91, 2014.

[100] P.-G. de Gennes, F. Brochard-Wyart, and D. Quere, *Capillarity and Wetting Phenomena: Drops, Bubbles, Pearls, Waves*. New York: Springer, 2002.

[101] L. G. J. Fokkink and J. Ralston, "Contact angles on charged substrates," *Colloids and Surfaces*, vol. 36, no. 1, pp. 69–76, 1989.

[102] G. Hanly, D. Fornasiero, J. Ralston, and R. Sedev, "Electrostatics and metal oxide wettability," *Journal of Physical Chemistry C*, vol. 115, pp. 14914–14921, aug 2011.

[103] H. Horiuchi, A. Nikolov, and D. Wasan, "Calculation of the surface potential and surface charge density by measurement of the three-phase contact angle," *Journal of Colloid and Interface Science*, vol. 385, pp. 218–224, nov 2012.

[104] J. Kaur and R. Kant, "Theory of Work Function and Potential of Zero Charge for Metal Nanostructured and Rough Electrodes," vol. 121, pp. 13059–13069, jun 2017.

[105] R. Jinnouchi and A. Anderson, "Electronic structure calculations of liquid-solid interfaces: Combination of density functional theory and modified Poisson-Boltzmann theory," *Physical Review B*, vol. 77, p. 245417, 2008.

[106] H. Michaelson, "The work function of the elements and its periodicity," *Journal of Appled Physics*, vol. 48, p. 4729, 1977.

[107] R. Doerner, M. Baldwin, M. Simmonds, J. Yu, L. Buzi, and T. Schwarz-Selinger, "Quantitatively measuring the influence of helium in plasma-exposed tungsten," *Nuclear Materials and Energy*, vol. 12, pp. 372–378, aug 2017.

[108] Q.-S. Chen, J. Solla-Gullon, S.-G. Sun, and J. Feliu, "The potential of zero total charge of Pt nanoparticles and polycrystalline electrodes with different surface structure: The role of anion adsorption in fundamental electrocatalysis," *Electrochimica Acta*, vol. 55, pp. 7982–7994, 2010.

[109] A. Di Paola, F. Di Quarto, and G. Serravalle, "A tensiostatic study of the anodic behaviour of tungsten in acid solutions," *Journal of the Less Common Metals*, vol. 42, pp. 315–324, oct 1975.

[110] P. R. Bandaru, H. Yamada, R. Narayanan, and M. Hoefer, "Charge transfer and storage in nanostructures," *Materials Science and Engineering R: Reports*, vol. 96, pp. 1–69, oct 2015.

[111] J. Huang, A. Malek, J. Zhang, and M. H. M. Eikerling, "No Title," *Journal of Physical Chemistry C*, vol. 120, pp. 13587–13595, 2016.

[112] P. Arosio and S. Levi, "No Title," *Free Radical Biology and Medicine*, vol. 33, pp. 457–463, aug 2002.

[113] J. L. J. Smith, "No Title," vol. 30, pp. 173–185, jan 2004.

[114] A. Camacho, X. Waletr, A. Picazo, J. Zopfi, X. A. Walter, A. Picazo, and J. Zopfi, "Photoferrotrophy: Remains of an Ancient Photosynthesis in Modern Environments," *Frontiers in Microbiology*, p. 323, mar 2017.

[115] M. M.-C. Carrier, J. J.-S. Bourassa, E. Massé, and E. Masse, "Cellular Homeostasis: A Small RNA at the Crossroads of Iron and Photosynthesis," *Current Biology*, vol. 27, pp. R380–R383, may 2017.

[116] D. Finazzi and P. Arosio, "Biology of ferritin in mammals: an update on iron storage, oxidative damage and neurodegeneration," 2014.

[117] R. Watt, R. Hilton, and D. Graff, "Oxido-reduction is not the only mechanism allowing ions to traverse the ferritin protein shell," *Biochimica et Biophysica Acta*, vol. 1800, pp. 745–759, 2010.

[118] G. Melman, F. Bou-Abdallah, E. Vane, P. Maura, P. Arosio, and A. Melman, "Iron release from ferritin by flavin nucleotides," *Biochimica et Biophysica Acta*, vol. 1830, pp. 4669–4674, 2013.

[119] E. C. E. Theil, R. K. R. Behera, and T. Tosha, "Ferritins for chemistry and for life," *Coordination Chemistry Reviews*, vol. 257, pp. 579–586, jan 2013.

[120] L. Toussaint, L. Bertrand, L. Hue, R. R. Crichton, and J.-P. P. Declercq, "High-resolution

X-ray Structures of Human Apoferritin H-chain Mutants Correlated with Their Activity and Metal-binding Sites," *Journal of Molecular Biology*, vol. 365, pp. 440–452, jan 2007.

[121] R. R. Crichton, *Iron metabolism : from molecular mechanisms to clinical consequences*. New York: John Wiley & Sons, Ltd., 2009.

[122] G. Jutz, P. Van Rijn, B. Santos Miranda, and A. Böker, "Ferritin: A versatile building block for bionanotechnology," 2015.

[123] D. Sharma and D. Bisht, "Role of Bacterioferritin & Ferritin in M. tuberculosis Pathogenesis and Drug Resistance: A Future Perspective by Interactomic Approach," *Frontiers in Cellular and Infection Microbiology*, vol. 7, p. 240, jun 2017.

[124] P. Foka, A. Dimitriadis, E. Karamichali, E. Kyratzopoulou, D. Giannimaras, J. Koskinas, A. Varaklioti, A. Mamalaki, and U. Georgopoulou, "Alterations in the iron homeostasis network: A driving force for macrophage-mediated hepatitis C virus persistency," *Virulence*, vol. 7, pp. 679–690, aug 2016.

[125] J. Tatur and W. R. Hagen, "The dinuclear iron-oxo ferroxidase center of Pyrococcus furiosus ferritin is a stable prosthetic group with unexpectedly high reduction potentials," *FEBS Letters*, vol. 579, pp. 4729–4732, aug 2005.

[126] J. Tatur, W. R. Hagen, and H. A. Heering, "Voltammetry of Pyrococcus furiosus ferritin: dependence of iron release rate on mediator potential," *Dalton Transactions*, vol. 0, p. 2837, mar 2009.

[127] B. Zhang, R. K. Watt, N. Gálvez, J. M. Domínguez-Vera, and G. D. Watt, "Rate of iron transfer through the horse spleen ferritin shell determined by the rate of formation of Prussian Blue and Fe-desferrioxamine within the ferritin cavity," *Biophysical Chemistry*, vol. 120, no. 2, pp. 96–105, 2006.

[128] C. Bernacchioni, S. Ciambellotti, E. Theil, and P. Turano, "Is His54 a gating residue for the ferritin ferroxidase site?," *Biochimica et Biophysica Acta*, vol. 1854, pp. 1118–1122, 2015.

[129] C. Bernacchioni, V. Ghini, E. C. Theil, and P. Turano, "Modulating the permeability of ferritin channels," *RSC Advances*, vol. 6, pp. 21219–21227, feb 2016.

[130] M. Mehlenbacher, M. Poli, P. Arosio, P. Santambrogio, S. Levi, N. D. Chasteen, and F. Bou-Abdallah, "Iron Oxidation and Core Formation in Recombinant Heteropolymeric Human Ferritins," *Biochemistry*, vol. 56, pp. 3900–3912, aug 2017.

[131] G. N. L. Jameson, R. F. Jameson, and W. Linert, "New insights into iron release from ferritin: direct observation of the neurotoxin 6-hydroxydopamine entering ferritin and reaching redox equilibrium with the iron core.," *Organic & biomolecular chemistry*, vol. 2, no. 16, pp. 2346–51, 2004.

[132] M.-H. Kim, "Higher-Order Derivative Polarography/Voltammetry for a Reversible Electron Transfer Coupled with a Follow-up Chemical Reaction," *Journal of The Electrochemical Society*, vol. 137, no. 12, p. 3815, 1990.